

Sign-Aware Multistate Jaccard Kernels and Geometry for Real and Complex-Valued Signals

Vineet Yadav¹

¹Jet Propulsion Laboratory, California Institute of Technology, Pasadena, CA, USA

Abstract

We introduce a sign-aware, multistate Jaccard/Tanimoto framework that extends overlap-based distances from nonnegative vectors and measures to arbitrary real- and complex-valued signals while retaining bounded metric and positive-semidefinite kernel structure. Formally, the construction is a set- and measure-theoretic geometry: signals are represented as atomic measures on a signed state space, and similarity is given by a generalized Jaccard overlap of these measures. Each signal is embedded into a nonnegative multistate representation, using positive/negative splits for real signals, Cartesian and polar decompositions for complex signals, and user-defined state partitions for refined regime analysis. Applying the Tanimoto construction to these embeddings yields a family of $[0, 1]$ distances that satisfy the triangle inequality and define positive-semidefinite kernels usable directly in kernel methods and graph-based learning. Beyond pairwise distances, we develop coalition analysis via Möbius inversion, which decomposes signal magnitude into nonnegative, additive contributions with exact budget closure across coalitions of signals. Normalizing the same embeddings produces probability measures on coordinate-state configurations, so that the distance becomes a monotone transform of total variation and admits a regime-intensity decomposition. The resulting construction yields a single, mechanistically interpretable distance that simultaneously provides bounded metric structure, positive-semidefinite kernels, probabilistic semantics, and transparent budget accounting within one sign-aware framework, supporting correlograms, feature engineering, similarity graphs, and other analytical tools in scientific and financial applications.

1 Introduction

Similarity measures and kernels constitute the geometry of modern machine learning, governing the performance of nearest-neighbor methods, kernel machines, Gaussian processes, and representation learning. In these settings, a rigorous notion of “closeness” must satisfy dual constraints: it must be mathematically well behaved (e.g., satisfy metric axioms or yield positive-semidefinite kernels) while remaining scientifically meaningful for the domain at hand.

Two distinct families of comparison dominate current practice. The first comprises geometric distances such as Euclidean and Mahalanobis distance (Mahalanobis, 1936), cosine similarity (Salton and McGill, 1983), and dynamic time warping (Sakoe and Chiba, 1978). These methods treat data as vectors in a continuous linear space, quantifying proximity through coordinate-wise error aggregation or angular alignment. They perform well when a signal is defined by its location and direction in \mathbb{R}^n , but they lack an intrinsic notion of set-theoretic overlap or mass conservation.

The second family descends from the Jaccard index (Jaccard, 1901) and a sequence of related overlap coefficients that were originally formulated on incidence or count data, not on an explicit notion of “mass”. Early set-based variants such as the coefficients of Kulczyński and the binary forms used by Rogers and Tanimoto (Kulczyński, 1927; Rogers and Tanimoto, 1960; Tanimoto, 1958) operate on incidence vectors in $\{0, 1\}^n \subset \mathbb{Z}^n$. Closely related overlap functionals for abundance or count tables were introduced by Czekanowski and Motyka in \mathbb{N}^n (Czekanowski, 1909; Motyka, 1947), and Ružička made the extension to general nonnegative vectors $x \in \mathbb{R}_{\geq 0}^n$ explicit (Ruzicka, 1958). Later, in computer vision, the same algebraic intersection pattern was applied to color histograms in $\mathbb{R}_{\geq 0}^n$ by Swain and Ballard (Swain and Ballard, 1991), again as a similarity between empirical histograms rather than as a measure-theoretic construction.

In all of these classical formulations, the index is a two-argument functional on a non-negative sequence space,

$$S : \mathcal{X}^n \times \mathcal{X}^n \rightarrow [0, 1],$$

where \mathcal{X} is typically $\{0, 1\}$, \mathbb{N} , or $\mathbb{R}_{\geq 0}$ depending on the application. Analyses involving many samples proceed via pairwise similarity matrices built from $S(A, B)$, rather than through a single multi-way or coalition-level overlap functional.

While pairwise similarities $S(A, B)$ are sufficient for many tasks, a growing class of problems demands *multi-way* comparison and budgeting. Examples include comparing ensembles of models for the same physical field, decomposing profit and loss across multiple firms or portfolios, or attributing precipitation across overlapping events or regions. In such settings, it is not enough to know that signals are pairwise similar; one needs a coalition-level decomposition that explains how total magnitude is shared among groups of signals.

In this paper we *reinterpret* the overlap formulas on $\mathbb{R}_{\geq 0}^n$ as acting on discrete mass distributions supported on a finite partition of a subset of \mathbb{C} , with masses taking values in $\mathbb{R}_{\geq 0}$. This mass-based, set- and measure-theoretic viewpoint is not present in the original references; it is the geometric formalization of these indices that we develop in this paper.

Because they retain the physical units of the data, such overlap measures are ubiquitous in ecology (Bray and Curtis, 1957), cheminformatics (Bajusz et al., 2015), and other fields like textual similarity (Broder, 1997) where absolute quantities carry meaning. However, existing analyses of the Jaccard and Tanimoto indices are predominantly restricted to sets, measures, and nonnegative vectors representing counts, intensities, or membership weights; they neither accommodate signed or complex signals nor provide explicit probabilistic or coalition-level budget interpretations. Historically, this limitation reflects the fact that these indices were designed to quantify overlap in the *presence* and *magnitude* of a phenomenon (e.g., species abundances, molecular fragments, shingle frequencies), not gains versus losses. Consequently, there was no notion of “mass loss” or negative contribution at a coordinate,

so negative or complex-valued entries simply did not arise in the modeling space.

Real-world signals, however, are rarely nonnegative. Positive and negative excursions typically encode different mechanisms: above- versus below-baseline flux anomalies, model under- versus over-prediction in residual analysis, upward versus downward moves in asset prices, gene up- versus down-regulation, or the real and imaginary parts of a complex waveform. Existing overlap measures, designed for nonnegative inputs, cannot distinguish whether two vectors swing in the same or opposite directions: they collapse $+x$ and $-x$ to the same absolute value. Correlation and cosine similarity, in turn, identify antipodal signals as “maximally similar,” even though one is just a sign flip of the other. None of these indices directly answers the question:

How much do two signed (or complex) signals agree once we pay attention to direction and regime?

From a modeling perspective this question arises immediately. In virtually any learning or inference pipeline we can write

$$z = M_\theta(x) + e, \quad (1)$$

where z denotes data, M_θ is a prediction or generative mechanism, and e is a residual or discrepancy signal. It is the structure of e that reveals how the model succeeds or fails: sustained positive excursions indicate systematic underprediction, negative excursions indicate overprediction, and deviations concentrated in particular regimes or time windows signal structural change or missing mechanisms. A single scalar loss $\|e\|$ or a correlation coefficient collapses this structure.

Desiderata. The aim of this paper is not to add one more distance to an already long list (see, e.g., Cha, 2007, Tables 1–9), but to obtain a single, reusable construction that simultaneously:

- (D1) is sign- and regime-aware: it distinguishes agreement in direction and between scientifically meaningful states (e.g., large loss / small loss / neutral / small gain / large gain);
- (D2) yields a bounded $[0, 1]$ metric and a positive-semidefinite kernel that plugs directly into standard ML machinery;
- (D3) supports exact budget accounting: nonnegative, additive decompositions of shared magnitude (or energy/occupancy) across coordinates and coalitions of signals, with no residual;
- (D4) admits a clear probabilistic semantics, so that distances can be interpreted as total-variation discrepancies between induced measures;
- (D5) extends naturally to complex-valued embeddings without losing any of the above.

Standard families offer some of these properties in isolation. For example, Wasserstein distances provide probabilistic interpretation (Villani, 2009), Jaccard/Tanimoto indices provide unit-preserving overlap (Bray and Curtis, 1957), and many kernels are PSD by design (Schölkopf and Smola, 2002). To our knowledge, however, none provides all of (D1)–(D5) within a single model-agnostic framework tailored to signed and complex signals.

Contributions. This paper makes two main contributions.

- (i) We lift the classical Jaccard/Tanimoto overlap family from nonnegative vectors and measures to arbitrary real- and complex-valued signals via sign-aware embeddings, while preserving bounded metric structure and positive-semidefinite kernel representations.
- (ii) We equip this overlap family with new probabilistic and budget interpretations: every embedded signal induces a normalized measure on coordinate-state atoms, so the resulting distance is a monotone transform of total variation, and Möbius inversion yields an exact nonnegative decomposition of L^1 magnitude across coalitions of signals.

We introduce a sign-aware, multistate Jaccard–Tanimoto framework that extends overlap-based thinking to real and complex signals whose sign and regime matter. The construction is based on a multistate embedding $\psi^{(K)}(A)$, which maps a signal A into a nonnegative tensor whose entries record a nonnegative moment (e.g., magnitude, energy) of A lying in each state at each index. States are user-defined intervals B_0, \dots, B_{K-1} on the real line (e.g., a neutral “noise” band plus moderate and extreme positive/negative deviations), and for complex signals we provide both Cartesian and polar decompositions. Applying the classical Tanimoto construction on these nonnegative embeddings yields a family of $[0, 1]$ distances d_{peak} that satisfy the triangle inequality and define positive-semidefinite kernels usable directly in kernel methods and graph-based learning. Normalizing the same embeddings produces probability measures on coordinate–state configurations, and inclusion–exclusion (Möbius inversion; see Rota (1964)) then decomposes magnitude into nonnegative, additive coalition budgets with exact closure.

Taken together, these properties provide a unified infrastructure for bounded metrics, positive-semidefinite kernels, probabilistic semantics, transparent budget accounting, and built-in regime and intensity separation, supporting sign-aware correlograms, feature engineering, similarity graphs, and coalition diagnostics in scientific, financial, and other machine learning applications.

The remainder of the paper proceeds as follows. Section 2 reviews existing metrics and kernels and introduces notation. Section 3 formalizes the sign-aware and multistate constructions, proves that the resulting distances are metrics and that the associated similarities define positive-semidefinite kernels, and extends the framework to complex-valued signals. Section 4 develops the coalition (Venn/Möbius) budgeting and probabilistic views. Section 6.1 illustrates the behavior of the distance and kernel on synthetic examples and sketches how the framework can serve as a base layer for sign-aware correlograms, variograms, feature engineering, and similarity graphs. Section 7 compares the peak-to-peak family with established distance measures and summarizes the distinctive combination of properties achieved by the proposed framework.

2 Overview of Metrics and Concepts

Table 1 provides a compact reference for notation used through Section 4. Unnormalized quantities (N, U_{peak}) preserve the physical units of the data, while normalized quantities ($J_{\text{peak}}, d_{\text{peak}}$) are dimensionless.

Table 1: Key notation and mathematical objects (through Section 4).

Symbol	Description	Reference
Sign structure		
$\text{sgn}(x)$	Sign function taking values in $\{-1, 0, +1\}$	Def. 3.3
Sign-split embedding		
x_i^+, x_i^-	Positive and negative parts: $x_i^+ = \max\{x_i, 0\}$, $x_i^- = \max\{-x_i, 0\}$	Def. 3.4
$\phi(X)$	Sign-split embedding $\phi : \mathbb{R}^n \rightarrow \mathbb{R}_{\geq 0}^{2n}$	Def. 3.4
Peak intersection, union, and similarity		
$\mathcal{I}_{\text{same}}(A, B)$	Index set where A and B share the same nonzero sign	Def. 3.7
$N(A, B)$	Sign-aware intersection (units preserved): overlap of same-signed excursions	Def. 3.8
$U_{\text{peak}}(A, B)$	Peak-to-peak union (units preserved): sum of half-wave maxima for the pair	Def. 3.9
$J_{\text{peak}}(A, B)$	Peak Jaccard coefficient: $N(A, B)/U_{\text{peak}}(A, B) \in [0, 1]$ (defined as 1 when $U_{\text{peak}}=0$)	Def. 3.10
$d_{\text{peak}}(A, B)$	Peak distance: $1 - J_{\text{peak}}(A, B) \in [0, 1]$	Def. 3.11
$K_{\text{peak}}(A, B)$	Peak kernel: $K_{\text{peak}}=J_{\text{peak}}$ is positive-semidefinite	Thm. 3.15
Multistate embedding and coalitions		
\mathcal{B}	Partition of \mathbb{R} : $\{B_0, \dots, B_{K-1}\}$ used in multistate embeddings	Def. 3.18
$\psi^{(K)}(X)$	Multistate norm-preserving embedding $\psi^{(K)} : \mathbb{R}^n \rightarrow \mathbb{R}_{\geq 0}^{n \times K}$ with respect to \mathcal{B}	Def. 3.18
$N(S)$	Cumulative multistate intersection (coalition budget) for $S \subseteq [m]$	Def. 4.1
$\widetilde{N}(S)$	Exclusive multistate intersection (Möbius-inverted budgets) for coalition S	Def. 4.2
Ω	Coordinate-state space indexing multistate atoms	Def. 4.9
ν_A	Finite measure on Ω induced by signal A	Def. 4.10
P_A	Normalized probability distribution on Ω induced by A	Def. 4.11
Metric and kernel properties		
Metric property: $d_{\text{peak}}=d_{\text{Tan}}(\phi(A), \phi(B))$		Thm. 3.12
Positive-semidefiniteness of K_{peak}		Thm. 3.15

Continued on next page

Table 1 (continued)

Symbol	Description	Reference
$d_{\text{multi}}(X, Y)$	Multistate Tanimoto distance $d_{\text{Tan}}(\psi^{(K)}(X), \psi^{(K)}(Y));$ metric on $\psi^{(K)}(\mathbb{R}^n)$, pseudometric on \mathbb{R}^n	Thm. 3.22
$K_{\text{multi}}(X, Y)$	Multistate Tanimoto kernel $J_{\text{Tan}}(\psi^{(K)}(X), \psi^{(K)}(Y)),$ positive- semidefinite on \mathbb{R}^n	Thm. 3.22
Generalized embeddings		
$\psi_C(Z)$	Cartesian embedding for complex signals (real/imaginary sign-split)	Def. 3.24
$\psi_P^{(K)}(Z)$	Polar embedding for complex signals (magnitude with phase partition)	Def. 3.24
Classical references		
$d_{\text{Tan}}, J_{\text{Tan}}$	Tanimoto distance and similarity on non-negative vectors; $d_{\text{Tan}}(x, y) = 1 - J_{\text{Tan}}(x, y)$ and $d_{\text{peak}} = d_{\text{Tan}} \circ \phi$ on embedded signals	Thm. 3.12, Lem. 3.14

Computational verification. To complement the analytic development in Sections 3 and 4, we implemented the full peak-to-peak framework in Python, including the sign-split embedding ϕ , the multistate embedding $\psi^{(K)}$, coalition Möbius inversion, the probabilistic TV/ δ representation, and the complex Cartesian extension ψ_C . For every worked example in the manuscript (Eqs. (39)–(40), (47)–(48), (57)–(65), (70)–(72), and (113)–(128)), the implementation reproduces the reported numerical values exactly. Monte Carlo experiments further confirm that (i) $d_{\text{peak}}(A, B)$ coincides with the min–max Tanimoto distance on $\phi(A), \phi(B)$; (ii) the real and complex kernels $K(A, B) = J_{\text{peak}}(A, B)$ and $K_{\psi_C}(Z_1, Z_2)$ produce positive-semidefinite Gram matrices; (iii) d_{peak} satisfies the triangle inequality and is invariant under common positive rescaling; and (iv) coalition budgets $\sum_{S \ni j} \tilde{N}(S)$ close numerically to $\|A_j\|_1$, and coarsening the state partition decreases the distance, in line with the data-processing interpretation. While not a substitute for formal proofs, these checks provide an independent, executable confirmation that the algebraic identities and structural properties in the sequel are correctly implemented and numerically stable.

3 Core Mathematical Properties

This section establishes the mathematical foundations of the sign-aware similarity framework, proving that the proposed measures constitute a proper metric and demonstrating their extension to multi-way comparisons.

3.1 Design axioms for signed excursions

Our construction ultimately applies to complex-valued signals $X \in \mathbb{C}^n$, but it operates on the real-valued excursions that arise from their real and imaginary parts. This decomposition is not merely algebraic; it respects the phenomenological reality that orthogonal components (real vs. imaginary) and opposing polarities (positive vs. negative) often represent distinct physical channels—such as in-phase vs. quadrature states or assets vs. liabilities—where structural alignment is semantically distinct from arithmetic cancellation. In this subsection we therefore formulate the basic requirements that any sign-aware overlap and union should satisfy for real-valued channels, and we state the axioms for $A, B \in \mathbb{R}^n$. The extension to complex-valued signals $X \in \mathbb{C}^n$ is obtained by applying the same construction separately to $\Re X$ and $\Im X$; coalition analyses for (A_1, \dots, A_m) are then performed by treating these real and imaginary components as distinct channels within the unified embedding space.

- (A1) **Sign locality.** Overlap and union are computed coordinatewise: the contribution at coordinate i depends only on the pair (A_i, B_i) and is independent of all other coordinates.
- (A2) **Excursion separation.** Positive and negative excursions are treated as disjoint channels. A coordinate with opposite signs, $A_i B_i < 0$, contributes zero overlap: only excursions with the same nonzero polarity can reinforce each other.
- (A3) **Magnitude monotonicity.** The overlap and union functionals should be non-decreasing with respect to magnitude at each coordinate. Specifically, if $|A_i|$ increases while its sign and B_i are held fixed, then the local contributions to the overlap $N(A, B)$ and the union $U_{\text{peak}}(A, B)$ at coordinate i should not decrease.
- (A4) **L^1 compatibility and reduction.** The total “mass” of a signal is measured by its L^1 norm, $\|A\|_1 = \sum_i |A_i|$. The overlap and union must respect this scale, satisfying $0 \leq N(A, B) \leq U_{\text{peak}}(A, B) \leq \|A\|_1 + \|B\|_1$. Furthermore, when $A, B \in \mathbb{R}_{\geq 0}^n$, the construction must reduce to the classical intersection and union operators underlying the Tanimoto and Jaccard indices.

The sign-split embedding in Definition 3.4, together with the overlap $N(A, B)$ in (8) and the peak-to-peak union $U_{\text{peak}}(A, B)$ in (9), constitutes a natural and minimal construction that satisfies axioms (A1)–(A4) while preserving the physical units of the data.

Remark 3.1 (Zero as a physical state). Our treatment of zero-valued excursions follows the same physical design principles. Zero is not interpreted as an algebraic indeterminacy of the form “0/0” arising in a normalized index; it is a bona fide physical state. Two identically zero signals correspond to the same state of the system and are therefore regarded as perfectly similar. Consistent with the normalization of the overlap and union, the resulting peak-to-peak similarity satisfies

$$J_{\text{peak}}(0, 0) = 1.$$

This behavior is physically meaningful in applications where zero encodes a distinct regime, for example:

- Mass = 0: “no mass present” in a control volume;
- Flux = 0: “perfect balance” with no net inflow or outflow;
- Rain = 0: “drought conditions” with complete absence of precipitation.

In all such cases, the absence of activity is a well-defined state in the geometry rather than an undefined limit.

Remark 3.2 (Semantic separation of channels). Axiom (A2) encodes the intuition that overlap is only meaningful within the same semantic channel. Positive excursions typically represent assets, gains, or production (e.g., portfolio value, gross primary productivity, revenue), whereas negative excursions represent losses, costs, or consumption (e.g., drawdowns, respiration, expenses). In such settings, it is natural to assert that “assets overlap with assets” and “losses overlap with losses,” but not that an asset overlaps with a loss. The sign-split embedding enforces this separation: only like-signed contributions reinforce each other in the overlap $N(A, B)$, while opposite-signed excursions are accounted for via the union $U_{\text{peak}}(A, B)$ and the resulting distance.

3.2 Foundational Definitions

We begin by formalizing the embedding that enables sign-aware comparisons while maintaining mathematical rigor.

Definition 3.3. For any real number $x \in \mathbb{R}$, we define the sign function as

$$\text{sgn}(x) := \begin{cases} +1 & \text{if } x > 0, \\ 0 & \text{if } x = 0, \\ -1 & \text{if } x < 0. \end{cases} \quad (2)$$

This function serves as the coordinate-wise mechanism for axiom **A1**: throughout this work, all comparisons and sign determinations employ this function locally at each index i . Consequently, the metric properties established in subsection 3.4 emerge from the aggregation of these independent local operations.

Definition 3.4 (Sign-split embedding). The sign-split embedding $\phi(X)$ realizes the **Excursion separation** axiom **A2** by transforming a real-valued signal into a non-negative representation that strictly separates positive and negative components. For a vector $X = (x_1, \dots, x_n) \in \mathbb{R}^n$, we define the embedding $\phi : \mathbb{R}^n \rightarrow \mathbb{R}_{\geq 0}^{2n}$ as

$$\phi(X) := (x_1^+, x_1^-, x_2^+, x_2^-, \dots, x_n^+, x_n^-), \quad (3)$$

where for each coordinate i ,

$$x_i^+ := \max\{x_i, 0\}, \quad x_i^- := \max\{-x_i, 0\}. \quad (4)$$

This decomposition ensures that each component x_i is represented by exactly one non-zero value in the pair (x_i^+, x_i^-) , enforcing the disjoint channel requirement of axiom **A2**. When

$x_i > 0$, the positive part x_i^+ captures its magnitude while $x_i^- = 0$. Conversely, when $x_i < 0$, the negative part x_i^- records $|x_i|$ while $x_i^+ = 0$. This alternating structure $(+, -)$ creates a doubled space where sign information is encoded through position rather than through the numerical sign itself. For example, if $x_i = -3$, then $(x_i^+, x_i^-) = (0, 3)$. If $x_i = 5$, then $(x_i^+, x_i^-) = (5, 0)$.

A key property of this embedding is that it preserves the signal's total magnitude, which is crucial for maintaining the physical units of the data. The following lemma formally establishes that this construction satisfies the mass conservation axiom.

Lemma 3.5 (L^1 -preservation of the sign-split embedding). *The sign-split embedding preserves the total magnitude of the signal. For every $X \in \mathbb{R}^n$,*

$$\|\phi(X)\|_1 = \|X\|_1. \quad (5)$$

Proof. By construction, the positive and negative parts satisfy the identity $|x_i| = x_i^+ + x_i^-$ for every coordinate i . Summing over all coordinates yields:

$$\|\phi(X)\|_1 = \sum_{i=1}^n (x_i^+ + x_i^-) = \sum_{i=1}^n |x_i| = \|X\|_1. \quad (6)$$

This explicitly confirms that the embedding ϕ satisfies the L^1 **compatibility** requirement of axiom **A4** \square

Remark 3.6. The preservation of the L^1 norm ensures that physical units and scale are maintained throughout the embedding process, as demanded by axiom **A4**. This property is also essential for the isometric relationship established in Theorem 3.12.

3.3 Pairwise Sign-Aware Measures

We now construct the specific overlap and union functionals that satisfy the design axioms of Section 3.1. By applying the classical intersection and union logic to the sign-split embedding $\phi(A)$, we obtain three building-block quantities: (i) a *sign-aware intersection* that realizes the excursion separation axiom, (ii) a *peak-to-peak union* that captures the full dynamic range, and (iii) the normalized similarity and distance derived from their ratio.

3.3.1 Sign-aware intersection

To satisfy the **Excursion separation** axiom **A2**, the intersection measure must quantify shared magnitude only where signals maintain directional consistency. This requires identifying coordinates where reinforcing polarities occur.

Definition 3.7 (Index set of sign agreement). For two signals $A, B \in \mathbb{R}^n$, the index set of sign agreement comprises all coordinates where both signals exhibit the same non-zero polarity:

$$\mathcal{I}_{\text{same}}(A, B) = \left\{ i \in \{1, \dots, n\} \mid \text{sgn}(A_i) = \text{sgn}(B_i) \neq 0 \right\}. \quad (7)$$

This set isolates the domain where signal reinforcement is physically meaningful, filtering out opposing contributions.

Definition 3.8 (Pairwise sign-aware intersection). The sign-aware intersection $N(A, B)$ is defined as the component-wise minimum of the sign-split embeddings, restricted to the set of sign agreement:

$$N(A, B) := \sum_{i \in \mathcal{I}_{\text{same}}(A, B)} \min(|A_i|, |B_i|). \quad (8)$$

This formulation enforces axiom **A2**: if A_i and B_i have opposite signs, $i \notin \mathcal{I}_{\text{same}}$ and the contribution is zero. Consistent with axiom **A4**, the measure preserves the physical units of the signal, representing the total magnitude shared by A and B within the same semantic channel.

3.3.2 Peak-to-peak union

To normalize the intersection, we require a union measure that respects the **Magnitude monotonicity** axiom **A3** bounds the L^1 norm. This is achieved by computing the envelope of the excursions in the sign-split space.

Definition 3.9 (Peak-to-peak union). For signals $A, B \in \mathbb{R}^n$, the peak-to-peak union is defined as the sum of the coordinate-wise maxima of the positive and negative parts:

$$U_{\text{peak}}(A, B) := \sum_{i=1}^n \left(\max\{A_i^+, B_i^+\} + \max\{A_i^-, B_i^-\} \right). \quad (9)$$

By taking the maximum of the sign-split components, U_{peak} captures the full dynamic range spanned by the signal pair. This definition satisfies axiom **A3** (since the maximum is monotonic) and axiom **A4** (L^1 compatibility) via the inequality $\max(x, y) \leq x + y$ for non-negative inputs, ensuring $U_{\text{peak}}(A, B) \leq \|A\|_1 + \|B\|_1$.

3.3.3 Similarity coefficient and distance

The ratio of the sign-aware intersection to the peak-to-peak union yields a normalized similarity coefficient analogous to the classical Jaccard index but adapted for signed data.

Definition 3.10 (Peak-to-peak similarity coefficient). The peak-to-peak similarity coefficient between signals A and B is

$$J_{\text{peak}}(A, B) := \begin{cases} \frac{N(A, B)}{U_{\text{peak}}(A, B)}, & \text{if } U_{\text{peak}}(A, B) > 0, \\ 1, & \text{if } U_{\text{peak}}(A, B) = 0. \end{cases} \quad (10)$$

From the construction of N and U_{peak} it follows that $0 \leq N(A, B) \leq U_{\text{peak}}(A, B)$, ensuring the coefficient ranges from 0 (no directional overlap) to 1 (perfect alignment in magnitude and sign).

Definition 3.11 (Peak-to-peak distance). The peak-to-peak distance is the complement of the similarity coefficient:

$$d_{\text{peak}}(A, B) := 1 - J_{\text{peak}}(A, B) \in [0, 1]. \quad (11)$$

3.4 Metric Properties

Building on the intersection $N(A, B)$ and union $U_{\text{peak}}(A, B)$ defined above, we now establish that the derived pairwise dissimilarity d_{peak} satisfies the metric axioms. The next theorem shows that d_{peak} coincides with the classical Tanimoto/Jaccard distance applied to the sign-split embeddings $\phi(A)$ and $\phi(B)$. This equivalence ensures that d_{peak} inherits all established metric properties from the well-studied Tanimoto distance.

Theorem 3.12 (Metric property of d_{peak}). *Let d_{peak} be defined from N and U_{peak} via Definitions 3.8, 3.9, 3.10, and 3.11, and let ϕ be the sign-split embedding of Definition 3.4. Then for all $A, B \in \mathbb{R}^n$,*

$$d_{\text{peak}}(A, B) = d_{\text{Tan}}(\phi(A), \phi(B)), \quad (12)$$

where d_{Tan} denotes the generalized Jaccard/Tanimoto distance on the nonnegative space $\mathbb{R}_{\geq 0}^{2n}$. For $U, V \in \mathbb{R}_{\geq 0}^{2n}$ this distance is given by

$$d_{\text{Tan}}(U, V) := 1 - J_{\text{Tan}}(U, V), \quad J_{\text{Tan}}(U, V) := \begin{cases} \frac{\sum_j \min\{U_j, V_j\}}{\sum_j \max\{U_j, V_j\}}, & \text{if } \sum_j \max\{U_j, V_j\} > 0, \\ 1, & \text{if } U = V = 0, \end{cases} \quad (13)$$

which is the usual min–max (“Tanimoto”) Jaccard similarity used on nonnegative vectors (see, e.g., Tripp et al. (2023)). It is known that the corresponding distance d_{Tan} is a metric on $\mathbb{R}_{\geq 0}^{2n}$; concise proofs are given by Kosub (2016) (see also the journal version (Kosub, 2019) and the classical references cited therein). Consequently, d_{peak} is a metric on \mathbb{R}^n .

Proof. The proof establishes that d_{peak} equals the classical Tanimoto distance applied to the embedded vectors $\phi(A)$ and $\phi(B)$, and therefore inherits the metric property.

Step 1 (Numerator identity). We first show that $N(A, B)$ equals the Tanimoto numerator for $(\phi(A), \phi(B))$. For any coordinate i , recall

$$A_i^+ = \max\{A_i, 0\}, \quad A_i^- = \max\{-A_i, 0\}, \quad (14)$$

and similarly for B_i^+, B_i^- . If A_i and B_i have the same nonzero sign or one of them is zero, then either both are nonnegative or both are nonpositive, and we have the identity

$$\min(|A_i|, |B_i|) = \min(A_i^+, B_i^+) + \min(A_i^-, B_i^-). \quad (15)$$

Indeed, if $A_i, B_i \geq 0$ then $A_i^- = B_i^- = 0$ and

$$\min(|A_i|, |B_i|) = \min(A_i, B_i) = \min(A_i^+, B_i^+), \quad (16)$$

while if $A_i, B_i \leq 0$ then $A_i^+ = B_i^+ = 0$ and

$$\min(|A_i|, |B_i|) = \min(|A_i|, |B_i|) = \min(A_i^-, B_i^-). \quad (17)$$

The same equality also holds when $A_i B_i = 0$ (one or both entries are zero), since both sides then equal 0. Thus (15) holds for all indices with $A_i B_i \geq 0$.

Crucially, when A_i and B_i have *opposite* signs we have $A_i B_i < 0$, and hence one of $\{A_i^+, B_i^+\}$ and one of $\{A_i^-, B_i^-\}$ is zero. In that case

$$\min(A_i^+, B_i^+) = 0 \quad \text{and} \quad \min(A_i^-, B_i^-) = 0, \quad (18)$$

so the right-hand side of (15) vanishes, even though $\min(|A_i|, |B_i|)$ need not be zero.

Let

$$\mathcal{I}_{\text{same}}(A, B) := \{i : A_i B_i > 0\}, \quad (19)$$

the sign-agreement index set from Definition 3.7. On this set (15) holds, and by definition

$$N(A, B) = \sum_{i \in \mathcal{I}_{\text{same}}(A, B)} \min(|A_i|, |B_i|). \quad (20)$$

Summing (15) over $i \in \mathcal{I}_{\text{same}}(A, B)$ gives

$$\sum_{i \in \mathcal{I}_{\text{same}}(A, B)} \min(|A_i|, |B_i|) = \sum_{i \in \mathcal{I}_{\text{same}}(A, B)} (\min(A_i^+, B_i^+) + \min(A_i^-, B_i^-)). \quad (21)$$

For indices with opposite signs, both minima on the right-hand side are zero, so we may extend the sum to all $i = 1, \dots, n$:

$$\sum_{i \in \mathcal{I}_{\text{same}}(A, B)} (\min(A_i^+, B_i^+) + \min(A_i^-, B_i^-)) = \sum_{i=1}^n (\min(A_i^+, B_i^+) + \min(A_i^-, B_i^-)). \quad (22)$$

The last equation is exactly the Tanimoto numerator for $(\phi(A), \phi(B))$, where ϕ is the sign-split embedding. This establishes that $N(A, B)$ equals the Tanimoto numerator for $(\phi(A), \phi(B))$.

Step 2 (Denominator identity). Let $U = \phi(A)$ and $V = \phi(B)$. The Tanimoto denominator for these embedded vectors is

$$\sum_j \max\{U_j, V_j\} = \sum_{i=1}^n (\max\{A_i^+, B_i^+\} + \max\{A_i^-, B_i^-\}), \quad (23)$$

which matches the definition of $U_{\text{peak}}(A, B)$ in (9). Thus $U_{\text{peak}}(A, B)$ equals the Tanimoto denominator for $(\phi(A), \phi(B))$.

Step 3 (Equality of coefficients). From Steps 1 and 2, both the numerator and denominator of $J_{\text{peak}}(A, B)$ coincide with those of $J_{\text{Tan}}(\phi(A), \phi(B))$, including the degenerate case where both are zero. Therefore

$$J_{\text{peak}}(A, B) = J_{\text{Tan}}(\phi(A), \phi(B)), \quad (24)$$

and by Definition 3.11 we obtain

$$d_{\text{peak}}(A, B) = d_{\text{Tan}}(\phi(A), \phi(B)), \quad (25)$$

which is exactly (12).

Step 4 (Metric transfer). Since ϕ is injective and d_{Tan} is a metric on $\mathbb{R}_{\geq 0}^{2n}$, the function d_{peak} inherits all metric properties: non-negativity, symmetry, identity of indiscernibles, and the triangle inequality. This completes the proof. \square

Remark 3.13 (Relation to Marczewski–Steinhaus and Kosub). Our construction is *not* a restatement of the Marczewski–Steinhaus normalized symmetric-difference metric. Their distance acts on sets (and, via indicator functions, on nonnegative functions) in the original measure space with a nonnegative measure μ (Marczewski and Steinhaus, 1958). In the same spirit, the modern treatments by Kosub (2016, 2019) work with nonnegative, monotone (sub)modular set functions and do not leave the nonnegative setting.

In their 1958 paper “On a certain distance of sets and the corresponding distance of functions Marczewski and Steinhaus (Marczewski and Steinhaus, 1958) introduce the set distance $\sigma(A, B) = \mu(A \Delta B)/\mu(A \cup B)$ on a σ -finite measure space (X, \mathcal{M}, μ) and show that (\mathcal{M}_0, σ) is a metric space (after identifying sets equal μ -a.e.) in their Section 1.2 “Metric σ ”, property (i). They then extend this construction to integrable (nonnegative) functions in Section 2.2, again establishing metricity (property (i)) for the induced function distance.

By contrast, the peak-to-peak distance is defined on arbitrary real (and complex) signals via the sign-split embedding ϕ , which lifts each $A \in \mathbb{R}^n$ to a nonnegative measure on an enlarged coordinate–sign space. This embedding is what makes sign-aware overlap, regime separation, and coalition budgeting possible; Marczewski and Steinhaus work entirely with sets (and their indicator functions) in the original measure space and do not address this signed/complex setting or the associated lattice geometry.

3.5 Positive-Semidefiniteness of the Kernel

The peak-to-peak similarity coefficient J_{peak} defines a kernel function $K_{\text{peak}} = J_{\text{peak}}$. We now establish that this kernel is positive semidefinite (PSD), ensuring its applicability in kernel-based machine learning methods including support vector machines, kernel principal component analysis, and Gaussian processes.

3.5.1 Framework and conventions

Throughout this section we work with the exact arithmetic version of J_{peak} and d_{peak} considered in Theorem 3.12, corresponding to the usual sign function and the raw values A_i, B_i . The sign-split embedding $\phi : \mathbb{R}^n \rightarrow \mathbb{R}_{\geq 0}^{2n}$ from Definition 3.4 maps each signal $X = (x_1, \dots, x_n)$ to interleaved pairs of positive and negative parts $(x_1^+, x_1^-, \dots, x_n^+, x_n^-)$. In the degenerate case where $U_{\text{peak}}(A, B) = 0$, which occurs exactly when $\phi(A) = \phi(B) = 0$ and hence $A = B = 0$, we assign $J_{\text{peak}}(A, B) = 1$ by convention, matching the usual definition of Tanimoto similarity on nonnegative vectors.

Lemma 3.14 (Identification with Tanimoto similarity on the embedding). *For all $A, B \in \mathbb{R}^n$, the peak-to-peak similarity equals the classical Tanimoto similarity applied to the embedded vectors $\phi(A), \phi(B) \in \mathbb{R}_{\geq 0}^{2n}$:*

$$J_{\text{peak}}(A, B) = \frac{\sum_{i=1}^n (\min\{A_i^+, B_i^+\} + \min\{A_i^-, B_i^-\})}{\sum_{i=1}^n (\max\{A_i^+, B_i^+\} + \max\{A_i^-, B_i^-\})} = J_{\text{Tan}}(\phi(A), \phi(B)). \quad (26)$$

Equivalently, indexing over the $2n$ components of the embedded vectors,

$$J_{\text{peak}}(A, B) = \frac{\sum_{j=1}^{2n} \min\{[\phi(A)]_j, [\phi(B)]_j\}}{\sum_{j=1}^{2n} \max\{[\phi(A)]_j, [\phi(B)]_j\}}. \quad (27)$$

Proof. By Definition 3.10 and Theorem 3.12, the numerator and denominator of $J_{\text{peak}}(A, B)$ coincide with those of the Tanimoto similarity $J_{\text{Tan}}(\phi(A), \phi(B))$: Step 1 of Theorem 3.12 shows that

$$N(A, B) = \sum_{i=1}^n (\min\{A_i^+, B_i^+\} + \min\{A_i^-, B_i^-\}), \quad (28)$$

while Step 2 shows that

$$U_{\text{peak}}(A, B) = \sum_{i=1}^n (\max\{A_i^+, B_i^+\} + \max\{A_i^-, B_i^-\}). \quad (29)$$

These are exactly the numerator and denominator of J_{Tan} applied to $\phi(A)$ and $\phi(B)$, with the same convention in the degenerate case $\phi(A) = \phi(B) = 0$. The equivalent expression in terms of the $2n$ coordinates of $\phi(A)$ and $\phi(B)$ follows by a simple reindexing of the sum. \square

Theorem 3.15 (Positive semidefiniteness of the peak-to-peak kernel). *The kernel function*

$$K_{\text{peak}}(A, B) = J_{\text{peak}}(A, B) \quad (30)$$

is positive semidefinite on \mathbb{R}^n . In particular, for any finite collection $\{A_1, \dots, A_m\} \subset \mathbb{R}^n$ and any coefficients $c_1, \dots, c_m \in \mathbb{R}$,

$$\sum_{i=1}^m \sum_{j=1}^m c_i c_j K_{\text{peak}}(A_i, A_j) \geq 0. \quad (31)$$

Proof. We establish positive semidefiniteness through the identification with the Tanimoto kernel and a standard kernel composition argument.

Step 1: Representation via positive and negative parts. From Lemma 3.14 we already have

$$N(A, B) = \sum_{i=1}^n (\min\{A_i^+, B_i^+\} + \min\{A_i^-, B_i^-\}), \quad (32)$$

$$U_{\text{peak}}(A, B) = \sum_{i=1}^n (\max\{A_i^+, B_i^+\} + \max\{A_i^-, B_i^-\}), \quad (33)$$

and hence

$$J_{\text{peak}}(A, B) = J_{\text{Tan}}(\phi(A), \phi(B)). \quad (34)$$

Step 2: Positive semidefiniteness of the Tanimoto/MinMax kernel. The Tanimoto/MinMax kernel

$$k_{\text{MinMax}}(u, v) := \frac{\sum_j \min\{u_j, v_j\}}{\sum_j \max\{u_j, v_j\}}, \quad u, v \in \mathbb{R}_{\geq 0}^d, \quad (35)$$

is known to be positive semidefinite on the nonnegative orthant $\mathbb{R}_{\geq 0}^d$ for any dimension d ; see Ralaivola et al. (2005, Def. 4, Eq. (8) and Prop. 6) for an explicit construction and proof (see also Tripp et al. (2023) for modern usage in cheminformatics). Consequently, for any finite collection $\{u_1, \dots, u_m\} \subset \mathbb{R}_{\geq 0}^d$ the Gram matrix $[k_{\text{MinMax}}(u_i, u_j)]_{ij}$ is positive semidefinite.

Step 3: Kernel composition preserves positive semidefiniteness. A standard result in kernel theory states that composing a positive semidefinite kernel with a fixed transformation preserves positive semidefiniteness (Schölkopf and Smola, 2002, Ch. 13, §13.1). Formally, if $k : \mathcal{X} \times \mathcal{X} \rightarrow \mathbb{R}$ is a positive semidefinite kernel and $\psi : \mathcal{Z} \rightarrow \mathcal{X}$ is any mapping, then

$$k'(z_1, z_2) = k(\psi(z_1), \psi(z_2)) \quad (36)$$

is positive semidefinite on \mathcal{Z} .

Applying this principle with $\mathcal{Z} = \mathbb{R}^n$, $\mathcal{X} = \mathbb{R}_{\geq 0}^{2n}$, $k = k_{\text{MinMax}}$, and $\psi = \phi$, and using (34), we obtain

$$K_{\text{peak}}(A, B) = J_{\text{peak}}(A, B) = k_{\text{MinMax}}(\phi(A), \phi(B)), \quad (37)$$

which is therefore positive semidefinite on \mathbb{R}^n as the composition of a positive semidefinite kernel with a fixed embedding. \square

Corollary 3.16 (Negative type of d_{peak}). *For any finite collection of signals $\{A_1, \dots, A_m\}$, let $S_{ij} := J_{\text{peak}}(A_i, A_j)$ and $d_{ij} := d_{\text{peak}}(A_i, A_j) = 1 - S_{ij}$. By Theorem 3.15, J_{peak} is a positive semidefinite kernel with $S_{ii} = 1$ and $0 \leq S_{ij} \leq 1$ for all i, j . By Theorem 6 of Gower and Legendre (1986), the dissimilarity matrix with entries $\sqrt{c(1 - S_{ij})}$ is Euclidean for any scalar $c > 0$; in particular, $\sqrt{d_{ij}} = \sqrt{1 - S_{ij}}$ is Euclidean. By Schoenberg's characterization of negative-type metrics (Schoenberg, 1935, Thm. 1), it follows that d_{peak} is of negative type.*

As a consequence, for any $\lambda > 0$ the radial kernel

$$K_\lambda(A, B) = \exp(-\lambda d_{\text{peak}}(A, B)) \quad (38)$$

is positive semidefinite, and d_{peak} admits an isometric embedding into a Hilbert space as a squared Euclidean distance.

Dual kernel structure. The peak-to-peak framework naturally yields two complementary kernels. First, the similarity

$$K_{\text{peak}}(A, B) := J_{\text{peak}}(A, B)$$

is positive semidefinite by Theorem 3.15, so for any finite collection of signals the matrix $[K_{\text{peak}}(A_i, A_j)]_{ij}$ is a valid Gram matrix. This kernel acts as a native overlap similarity: it measures how much mass A and B share in the same sign and state, and thus plays an analogous role to a linear or cosine kernel in conventional feature spaces.

Second, the associated distance $d_{\text{peak}}(A, B) = 1 - J_{\text{peak}}(A, B)$ is not itself positive semidefinite when used as a kernel matrix—a generic feature of nontrivial distance matrices with zero diagonals—but, as shown in Corollary 3.16, d_{peak} is of negative type. By Schoenberg's theorem, this implies that for every $\lambda > 0$ the radial kernel

$$K_\lambda(A, B) := \exp(-\lambda d_{\text{peak}}(A, B)) \quad (39)$$

is positive semidefinite. Thus d_{peak} generates a whole family of Gaussian/RBF-type kernels on the same signal space.

Together, K_{peak} provides a bounded, unit-preserving overlap kernel, while the K_λ family provides neighbourhood kernels for interpolation, regression, and manifold learning. Both are Hilbert-space kernels derived from the same underlying lattice geometry, a comparatively rare situation for a bounded, overlap-based metric.

3.5.2 Properties and implications

The positive semidefiniteness of K_{peak} established in Theorem 3.15 has several important theoretical and practical consequences.

Positive semidefiniteness versus strict positive definiteness. The kernel K_{peak} yields positive semidefinite Gram matrices, i.e., all eigenvalues are nonnegative but some may vanish. Zero eigenvalues arise whenever signals become linearly dependent after the embedding ϕ . This includes obvious cases such as duplicated signals, but also more structured dependencies (e.g., exact scalar multiples) that survive the sign-split transform. In numerical settings, additional rank deficiency may appear if very small coordinates are thresholded to zero so that signals differing only below machine precision collapse to the same embedded vector. Such behaviour is standard for positive semidefinite kernels and reflects redundancy or limited resolution in the data rather than any defect of the kernel. In practice, kernel methods handle singular Gram matrices via regularization or by restricting to the span of nonzero eigenvalues.

Role of the sign-split embedding. The sign-split transform ϕ is essential for extending the Tanimoto kernel to signed data. It preserves L^1 magnitude while encoding direction through positional structure: a positive entry $x_i > 0$ contributes x_i to the “+” channel and zero to the “-” channel, and conversely for negative entries. This separation allows the MinMax/Tanimoto kernel on $\mathbb{R}_{\geq 0}^{2n}$ to distinguish reinforcing excursions (same sign, which contribute to the intersection) from opposing excursions (opposite sign, which contribute only to the union). The classical Tanimoto kernel J_{Tan} is defined and known to be positive semidefinite on nonnegative vectors; applying it directly to signed inputs would break the conditions required for kernel validity. The embedding ϕ therefore acts as a bridge: it lifts real-valued signals into a nonnegative space where the MinMax kernel is valid, and kernel composition then transports positive semidefiniteness back to the original signal space.

Treatment of degenerate cases. In the exact theoretical setting, the degenerate case $U_{\text{peak}}(A, B) = 0$ occurs if and only if $\phi(A) = \phi(B) = 0$, i.e., $A = B = 0$. In this situation we set $J_{\text{peak}}(A, B) = 1$, matching the usual convention for Tanimoto similarity on nonnegative vectors. In numerical implementations, coordinates with magnitude below a fixed tolerance are typically rounded to zero; two signals whose entries are all numerically negligible will then be treated as perfectly similar. This only affects diagonal or near-diagonal entries of the Gram matrix and does not interfere with positive semidefiniteness.

Example 3.17 (Degenerate covariance under zero shared mass). Consider three scalar channels constructed from a short signal, e.g. the pattern $[2, 0, 1]$ under suitable centering and rescaling. The classical Pearson covariance (or correlation) matrix for these channels can take the schematic form

$$\Sigma = \begin{pmatrix} 1 & 0 & \rho \\ 0 & 1 & 0 \\ \rho & 0 & 1 \end{pmatrix}, \quad 0 < \rho < 1,$$

in which the middle channel appears orthogonal to the others. This happens because every time channels 1 or 3 move away from zero, channel 2 remains at zero, so the *shared variance* with channel 2 is identically zero.

In this Euclidean geometry, both situations $(A_i, B_i) = (0, 0)$ (vacuum vs. vacuum) and $(A_i, B_i) = (0, \neq 0)$ (vacuum vs. mass) contribute equally “nothing” to the covariance. Our mass-based construction separates these cases: vacuum is a well-defined physical state, so $(0, 0)$ is treated as perfectly similar ($J_{\text{peak}}(0, 0) = 1$), whereas $(0, \neq 0)$ contributes to the union but not to the overlap. This avoids the degeneracy where covariance treats “no shared mass” as geometrically indistinguishable from “shared vacuum”.

Distinction from subset-based approaches. Our route to positive semidefiniteness differs from classical set-theoretic treatments of Jaccard-type similarities. Some prior work (e.g., Bouchard et al., 2013) establishes positive semidefiniteness for Jaccard-like similarities on finite sets by indexing matrices over all subsets and analysing their spectra via combinatorial arguments. In that setting, objects are characterized purely by membership patterns and overlap is a function of set cardinalities.

By contrast, the present framework operates directly on continuous signals with quantitative magnitudes. Positive semidefiniteness is obtained by observing that the sign-split embedding ϕ converts each signed signal into a nonnegative vector and then invoking the known kernel property of the MinMax/Tanimoto similarity on $\mathbb{R}_{\geq 0}^d$ together with the fact that kernel composition preserves positive semidefiniteness. This pathway accommodates arbitrary dimensions and magnitudes, requires no reduction to subset indicators, and extends naturally to the multi-way and complex-valued generalizations developed below. The continuous, magnitude-aware nature of the construction also ensures that small perturbations in signal values produce correspondingly small changes in similarity, a stability property that discrete subset-based methods do not guarantee by default.

3.6 Generalization to Multistate Partitions

The sign-split embedding of Definition 3.4 partitions the real line into precisely two regions separated by the tolerance threshold, mapping each coordinate to either its positive or negative component while preserving magnitude. This binary structure, while sufficient for distinguishing directional agreement from opposition, represents only the simplest instance of a far more general construction. Many applications demand finer categorical resolution: financial analysts distinguish between modest and substantial gains, climatologists differentiate among degrees of temperature anomaly, and chemists recognize gradations of acidity rather than mere departure from neutrality. The framework naturally accommodates such

refinements through arbitrary measurable partitions of \mathbb{R} , each partition element capturing a distinct qualitative state while the embedded representation continues to preserve quantitative magnitude information within each state. For precision, we take partitions to be collections of pairwise disjoint measurable sets whose union is \mathbb{R} up to measure-zero boundaries; endpoints at thresholds are assigned consistently (e.g., right-closed on the positive side, left-closed on the negative side) to avoid overlap.

Definition 3.18 (Multistate norm-preserving embedding). Let $\mathcal{B} = \{B_0, \dots, B_{K-1}\}$ be a partition of \mathbb{R} into K disjoint measurable sets whose union is \mathbb{R} (up to measure-zero boundaries). For a signal $X = (x_1, \dots, x_n) \in \mathbb{R}^n$, the multistate norm-preserving embedding $\psi^{(K)} : \mathbb{R}^n \rightarrow \mathbb{R}_{\geq 0}^{n \times K}$ is defined by

$$[\psi^{(K)}(X)]_{i,k} = |x_i| \cdot \mathbf{1}\{x_i \in B_k\}, \quad i = 1, \dots, n, \quad k = 0, \dots, K-1, \quad (40)$$

where $\mathbf{1}\{\cdot\}$ denotes the indicator function.

The embedding represents X as an $n \times K$ matrix in which each row corresponds to a coordinate of the original signal and each column corresponds to a partition element. Because $\{B_k\}_{k=0}^{K-1}$ forms a partition, for each index i there exists exactly one k such that $x_i \in B_k$ (up to a boundary convention), ensuring that each row contains exactly one nonzero entry equal to $|x_i|$. Consequently, the embedding preserves the L^1 norm:

$$\|\psi^{(K)}(X)\|_1 = \sum_{i=1}^n \sum_{k=0}^{K-1} |x_i| \cdot \mathbf{1}\{x_i \in B_k\} = \sum_{i=1}^n |x_i| = \|X\|_1. \quad (41)$$

Remark 3.19 (Sign-awareness and the role of the partition). At first sight there appears to be a tension between the goal of constructing a sign-aware framework and the general multistate embedding $\psi^{(K)}$, which is defined for an arbitrary partition $\mathcal{B} = \{B_0, \dots, B_{K-1}\}$ of \mathbb{R} . This is best understood as a modelling choice rather than a contradiction.

The framework as a whole is sign-aware whenever the partition is chosen to respect sign (for example, with separate negative and positive bins and an optional neutral band). In contrast, the multistate embedding $\psi^{(K)}$ itself is agnostic to how the sets $\{B_k\}$ are chosen: if one deliberately uses bins that mix positive and negative values, then one is explicitly telling the framework *not* to distinguish those signs within that bin. In such cases the embedding $\psi^{(K)}$ is no longer injective on \mathbb{R}^n , and the induced distance d_{multi} is only a pseudometric there.

Thus there is no logical contradiction between proposing a sign-aware framework and allowing general multistate partitions. Rather, sign-awareness in the multistate setting depends on the partition: d_{multi} is sign-aware only when the partition separates sign (up to a neutral band), whereas sign-mixing bins deliberately collapse positive and negative values within the same state.

Example 3.20 (Multistate partition for financial applications). Consider financial return data where analysts distinguish five qualitative regimes. We establish a threshold $\tau > 0$ to demarcate moderate from extreme market movements. The partition $\mathcal{B} = \{B_0, B_1, B_2, B_3, B_4\}$

classifies returns according to

$$\begin{aligned}
B_0 &= \{0\}, \quad (\text{Neutral}) \\
B_1 &= (\tau, \infty), \quad (\text{Large Profit}) \\
B_2 &= (0, \tau], \quad (\text{Small Profit}) \\
B_3 &= [-\tau, 0), \quad (\text{Small Loss}) \\
B_4 &= (-\infty, -\tau). \quad (\text{Large Loss})
\end{aligned} \tag{42}$$

This partition exhibits symmetry about zero, isolates the exact-zero neutral state consistent with standard sign conventions, and employs the threshold τ to capture application-specific notions of materiality.

To illustrate the embedding mechanics, consider a 5-day return sequence $X \in \mathbb{R}^5$ analyzed with $\tau = 2.0$, with components

$$X = (8.2, 0.3, 0.0, -1.5, -5.1). \tag{43}$$

The component classifications proceed as follows: $x_1 = 8.2 > \tau$ belongs to B_1 (Large Profit); $x_2 = 0.3 \in (0, \tau]$ falls within B_2 (Small Profit); $x_3 = 0.0$ resides exactly in B_0 (Neutral); $x_4 = -1.5 \in [-\tau, 0)$ occupies B_3 (Small Loss); and $x_5 = -5.1 < -\tau$ enters B_4 (Large Loss).

The multistate embedding $\psi^{(5)} : \mathbb{R}^5 \rightarrow \mathbb{R}_{\geq 0}^{5 \times 5}$ produces the following matrix representation:

$$\psi^{(5)}(X) = \begin{pmatrix} 0 & 8.2 & 0 & 0 & 0 \\ 0 & 0 & 0.3 & 0 & 0 \\ 0 & 0 & 0 & 0 & 0 \\ 0 & 0 & 0 & 1.5 & 0 \\ 0 & 0 & 0 & 0 & 5.1 \end{pmatrix} \in \mathbb{R}_{\geq 0}^{5 \times 5}. \tag{44}$$

Each row contains at most one nonzero entry positioned in the column corresponding to that observation's qualitative state, with the entry's value equal to the absolute value of the original observation. The third row remains entirely zero since $|x_3| = 0$, illustrating that zero-magnitude observations produce zero contributions regardless of their state assignment. The total embedded mass $\|\psi^{(5)}(X)\|_1 = 8.2 + 0.3 + 0 + 1.5 + 5.1 = 15.1$ equals $\|X\|_1$, confirming norm preservation.

Remark 3.21 (Relationship to binary sign-split embedding). The sign-split embedding ϕ introduced in Definition 3.4 emerges as the minimal instantiation of this multistate framework, corresponding to $K = 2$ with partition elements $B_0 = (0, \infty)$ and $B_1 = (-\infty, 0]$, where the boundary point zero is assigned to the negative partition by convention. In applied settings, practitioners may introduce a tolerance band $[-\eta, \eta]$ around zero, treating values within this band either as a distinct neutral state or as numerically indistinguishable from zero, depending on the scientific context. The multistate framework accommodates various partitioning schemes including uniform quantization, percentile-based divisions, and domain-specific categories, while preserving the continuous magnitude information within each qualitative category and enabling similarity computations that respect both categorical boundaries and quantitative differences.

Theorem 3.22 (Metric and kernel properties of multistate embeddings). *Let $\psi^{(K)} : \mathbb{R}^n \rightarrow \mathbb{R}_{\geq 0}^{n \times K}$ be the multistate embedding of Definition 3.18. Then the Tanimoto distance composed with $\psi^{(K)}$,*

$$d_{\text{multi}}(X, Y) := d_{\text{Tan}}\left(\psi^{(K)}(X), \psi^{(K)}(Y)\right), \quad (45)$$

is a metric on the image $\psi^{(K)}(\mathbb{R}^n)$ and hence a pseudometric on \mathbb{R}^n . The associated Tanimoto kernel

$$K_{\text{multi}}(X, Y) := J_{\text{Tan}}\left(\psi^{(K)}(X), \psi^{(K)}(Y)\right) \quad (46)$$

is positive-semidefinite on \mathbb{R}^n .

Proof. The embedding $\psi^{(K)}$ maps into $\mathbb{R}_{\geq 0}^{n \times K}$, which we identify with $\mathbb{R}_{\geq 0}^{nK}$ via vectorization. On this space the Tanimoto distance is a known metric and the Tanimoto kernel is positive-semidefinite. Thus d_{Tan} is a metric on $\psi^{(K)}(\mathbb{R}^n)$, and the composed distance d_{multi} is a pseudometric on \mathbb{R}^n obtained by pulling back this metric along $\psi^{(K)}$. Positive-semidefiniteness of K_{multi} follows from the standard fact that composing a positive-semidefinite kernel with a fixed embedding preserves positive-semidefiniteness, as in Theorem 3.15. \square

Remark 3.23. In practice, signals that map to the same embedded representation under $\psi^{(K)}$ are indistinguishable at the chosen resolution, so the metric behaviour on \mathbb{R}^n simply reflects this modelling choice; on the induced quotient space where such signals are identified, the distance is a genuine metric.

3.7 Extension to Complex-Valued Signals

The sign-aware framework developed thus far operates on real-valued signals, distinguishing positive from negative excursions along a single axis. Complex-valued signals, by contrast, inhabit a two-dimensional space where each observation possesses both magnitude and phase, encoding information in angular position rather than merely in signed distance from zero. Such signals arise ubiquitously in frequency-domain representations obtained through Fourier analysis, in electromagnetic field measurements where electric and magnetic components couple through phase relationships, in quantum mechanical wavefunctions where probability amplitudes require complex representation, and in communications systems where information is modulated onto both in-phase and quadrature channels. The extension of our similarity framework to \mathbb{C}^n requires careful consideration of how directional agreement manifests in the complex plane, leading naturally to two complementary embedding strategies that respect either the Cartesian or polar structure of complex numbers.

The goal of an extension to \mathbb{C}^n is thus to quantify overlap in a way that respects the physical meaning of phase. For example, in comparing two quantum superposition states $Z = \psi_1 + \psi_2$ and $W = \psi_1 + e^{i\theta}\psi_2$, the polar embedding (Def. 3.24) must be able to capture the similarity (or lack thereof) introduced by the relative phase θ , which governs all interference phenomena. Likewise, in comparing I/Q communication signals, the Cartesian embedding (Def. 3.24) is required to respect the sign structure of both the real and imaginary channels independently, as each carries distinct information.

Definition 3.24 (Complex embeddings). Let $Z = (z_1, \dots, z_n) \in \mathbb{C}^n$ be a complex-valued signal. Write each component in both rectangular and polar form,

$$z_i = a_i + ib_i = r_i e^{i\phi_i}, \quad (47)$$

where $a_i, b_i \in \mathbb{R}$ denote the real and imaginary parts, $r_i = |z_i| \geq 0$ is the modulus, and $\phi_i \in (-\pi, \pi]$ is the principal argument.

Cartesian sign-split embedding. Treat the real and imaginary components as independent real-valued signals and apply the sign-split operation to each coordinate:

$$\psi_C(Z) := (a_1^+, a_1^-, b_1^+, b_1^-, \dots, a_n^+, a_n^-, b_n^+, b_n^-) \in \mathbb{R}_{\geq 0}^{4n}, \quad (48)$$

where

$$a_i^+ := \max\{a_i, 0\}, \quad a_i^- := \max\{-a_i, 0\}, \quad b_i^+ := \max\{b_i, 0\}, \quad b_i^- := \max\{-b_i, 0\}.$$

Each complex coordinate z_i thus generates four nonnegative components: the positive and negative parts of its real part, followed by the positive and negative parts of its imaginary part. This embedding preserves the natural rectangular structure $\mathbb{C} \cong \mathbb{R}^2$ and satisfies

$$|a_i| + |b_i| = a_i^+ + a_i^- + b_i^+ + b_i^- \quad \text{for each } i, \quad (49)$$

so that the total embedded L^1 mass equals the sum of absolute real and imaginary parts.

Polar phase-partition embedding. Partition the angular domain $(-\pi, \pi]$ into K disjoint sectors $\{\Theta_1, \dots, \Theta_K\}$ with a fixed, consistent boundary convention (e.g., left-open/right-closed intervals), and classify each complex number according to its phase angle. Define

$$[\psi_P^{(K)}(Z)]_{i,k} := r_i \mathbf{1}\{\phi_i \in \Theta_k\}, \quad (50)$$

where $r_i = |z_i|$ and ϕ_i is the principal argument of z_i . The resulting embedding maps Z to an $n \times K$ matrix in $\mathbb{R}_{\geq 0}^{n \times K}$, where each row contains the modulus r_i in the column corresponding to the angular sector containing ϕ_i , with zeros elsewhere. When $z_i = 0$ (so $r_i = 0$), the entire i -th row is zero. This representation respects the polar structure of complex numbers and yields a K -fold expansion of dimension determined by the chosen angular resolution.

Example 3.25 (Cartesian embedding of complex signals). Consider a discrete Fourier coefficient sequence $Z = (3+4i, -2+i, 1-2i) \in \mathbb{C}^3$ arising from spectral analysis. The Cartesian sign-split embedding decomposes each coefficient into its four signed components. For the first coefficient $z_1 = 3+4i$, the real part $a_1 = 3$ contributes $(a_1^+, a_1^-) = (3, 0)$ and the imaginary part $b_1 = 4$ contributes $(b_1^+, b_1^-) = (4, 0)$. The second coefficient $z_2 = -2+i$ has a negative real part yielding $(a_2^+, a_2^-) = (0, 2)$ and a positive imaginary part yielding $(b_2^+, b_2^-) = (1, 0)$. The third coefficient $z_3 = 1-2i$ produces $(a_3^+, a_3^-) = (1, 0)$ and $(b_3^+, b_3^-) = (0, 2)$. The complete embedding arranges these components sequentially:

$$\psi_C(Z) = (3, 0, 4, 0, 0, 2, 1, 0, 1, 0, 0, 2) \in \mathbb{R}_{\geq 0}^{12}. \quad (51)$$

This representation enables similarity comparisons that respect sign agreement separately in the real and imaginary dimensions, naturally accommodating applications where these components represent distinct physical quantities such as in-phase and quadrature signal channels.

Example 3.26 (Polar embedding of complex signals). Consider the same coefficient sequence $Z = (3 + 4i, -2 + i, 1 - 2i)$ but now emphasize phase relationships through a polar embedding. Partition the angular domain into four quadrants with a consistent endpoint convention: $\Theta_1 = (0, \pi/2]$ (first quadrant), $\Theta_2 = (\pi/2, \pi]$ (second quadrant), $\Theta_3 = (-\pi, -\pi/2]$ (third quadrant), and $\Theta_4 = (-\pi/2, 0]$ (fourth quadrant).

The first coefficient $z_1 = 3 + 4i$ has modulus $r_1 = \sqrt{9 + 16} = 5$ and argument $\phi_1 = \arctan(4/3) \approx 0.927$ radians, placing it in Θ_1 . The second coefficient $z_2 = -2 + i$ has modulus $r_2 = \sqrt{4 + 1} = \sqrt{5}$ and argument $\phi_2 = \pi - \arctan(1/2) \approx 2.678$ radians, locating it in Θ_2 . The third coefficient $z_3 = 1 - 2i$ has modulus $r_3 = \sqrt{1 + 4} = \sqrt{5}$ and argument $\phi_3 = -\arctan(2) \approx -1.107$ radians, positioning it in Θ_4 . With $K = 4$, the polar embedding becomes:

$$\psi_P^{(4)}(Z) = \begin{pmatrix} 5 & 0 & 0 & 0 \\ 0 & \sqrt{5} & 0 & 0 \\ 0 & 0 & 0 & \sqrt{5} \end{pmatrix} \in \mathbb{R}_{\geq 0}^{3 \times 4}. \quad (52)$$

This representation treats signals with similar phase angles as directionally aligned regardless of their Cartesian decomposition, making it particularly suitable for applications such as modal analysis where eigenvector phase relationships determine structural behavior, or communications systems where constellation points are organized by angular position.

Remark 3.27 (Choice of embedding strategy). The selection between Cartesian and polar embeddings depends on the physical interpretation of the complex data. The Cartesian approach ψ_C preserves the independence of real and imaginary components, making it natural when these components represent distinct measurable quantities—for instance, the electric field components E_x and E_y in electromagnetic analysis, or the in-phase I and quadrature Q channels in digital communications. This embedding imposes a four-fold dimensional expansion but maintains direct correspondence with the underlying physical variables.

The polar approach $\psi_P^{(K)}$ emphasizes angular relationships over Cartesian structure, treating complex numbers as magnitude-weighted phase indicators. The dimensional expansion factor K is user-specified, with smaller K providing coarse angular resolution (e.g., $K = 4$ for quadrant-level discrimination) and larger K enabling fine phase distinctions (e.g., $K = 16$ for 22.5° angular bins). When $z_i = 0$, the corresponding row of $\psi_P^{(K)}(Z)$ is all zeros. This embedding suits applications where phase coherence determines similarity, such as comparing Fourier spectra where resonance frequencies manifest as peaks with specific phase relationships, or analyzing quantum wavefunctions where relative phase governs interference phenomena. The choice of partition granularity K should balance angular resolution against dimensional tractability, with the understanding that excessively fine partitions may amplify sensitivity to phase noise without providing meaningful discrimination.

Theorem 3.28 (Metric and kernel properties for complex signals). *Let ψ_C and $\psi_P^{(K)}$ be the complex embeddings from Definition 3.24. Then, for each embedding $\psi \in \{\psi_C, \psi_P^{(K)}\}$, the Tanimoto distance*

$$d_\psi(Z, W) := d_{\text{Tan}}(\psi(Z), \psi(W)) \quad (53)$$

is a metric on the image $\psi(\mathbb{C}^n)$ and hence a pseudometric on \mathbb{C}^n . The associated Tanimoto kernel

$$K_\psi(Z, W) := J_{\text{Tan}}(\psi(Z), \psi(W)) \quad (54)$$

is positive-semidefinite on \mathbb{C}^n .

Proof. Each embedding ψ maps \mathbb{C}^n into a nonnegative Euclidean space: $\psi_C(\mathbb{C}^n) \subset \mathbb{R}_{\geq 0}^{4n}$ and $\psi_P^{(K)}(\mathbb{C}^n) \subset \mathbb{R}_{\geq 0}^{nK}$. On these nonnegative spaces the Tanimoto distance is a metric and the Tanimoto similarity is a positive-semidefinite kernel (see, e.g., Ralaivola et al. (2005); Tripp et al. (2023)). Hence d_{Tan} is a metric on each image $\psi(\mathbb{C}^n)$, and the pulled-back distance $d_\psi(Z, W) = d_{\text{Tan}}(\psi(Z), \psi(W))$ is a pseudometric on \mathbb{C}^n . Positive-semidefiniteness of K_ψ follows from the standard result that composing a positive-semidefinite kernel with a fixed embedding preserves positive-semidefiniteness, as in Theorem 3.15. \square

Remark 3.29 (Metric behavior). For the Cartesian embedding ψ_C , the map $\psi_C : \mathbb{C}^n \rightarrow \mathbb{R}_{\geq 0}^{4n}$ is injective: each coordinate $z_i = a_i + ib_i$ is uniquely recovered from $(a_i^+, a_i^-, b_i^+, b_i^-)$. In this case the induced distance d_{ψ_C} is a genuine metric on \mathbb{C}^n . For the polar embedding $\psi_P^{(K)}$, different signals whose components share the same moduli and fall into the same angular sectors may map to the same embedded representation, so $d_{\psi_P^{(K)}}$ is generally only a pseudometric. In practice, signals that map to the same embedded representation are indistinguishable at the chosen angular resolution, so the metric behavior on \mathbb{C}^n simply reflects this modeling choice; on the induced quotient space where such signals are identified, the distance is a genuine metric.

4 Multistate Coalition Analysis and Dimensional Reduction

The pairwise similarity framework developed in the preceding sections extends naturally to comparisons involving multiple signals simultaneously. Such multi-way comparisons arise when analyzing portfolios of time series, ensembles of climate model outputs, or collections of spectral measurements where we seek to quantify the shared behavior across all members rather than merely examining pairs. Moving from pairwise to multi-way analysis introduces two conceptual choices that shape both the interpretation and the computational structure of the resulting measures.

The first choice concerns how much of the original signal magnitude we carry into the coalition analysis. In the multistate setting, each coordinate of a signal is assigned to exactly one state B_k in a partition $\mathcal{B} = \{B_0, \dots, B_{K-1}\}$ of \mathbb{R} , with one state (often denoted B_0) playing the role of a *neutral* category. Treating this neutral state on the same footing as the other states leads to an embedding in which the full L^1 norm of each signal is preserved: every unit of magnitude belongs to exactly one coordinate-state atom. This choice is essential for coalition accounting, because it allows us to decompose each signal's total norm into non-overlapping contributions associated with different coalitions, with no residual mass left unassigned. In this section we adopt this fully norm-preserving multistate embedding and use it as the basis for defining cumulative and exclusive intersections across coalitions.

The second choice involves the granularity of the state partition. A fine multistate partition (such as distinguishing large losses, small losses, neutral, small gains, and large gains) provides detailed information about where overlap occurs, but practical applications often require simpler summaries. We show that a coarse two-state view (positive versus negative,

with neutral optionally reported separately) can be recovered from fine-grained multistate calculations through principled aggregation, avoiding the need to perform separate analyses at different resolutions. This dimensional reduction must be performed carefully: aggregating state channels *before* computing coordinatewise minima can produce incorrect results, whereas aggregating *after* computing per-state, per-coordinate minima preserves the intersection structure exactly.

Throughout this section, we consider m signals $A_1, \dots, A_m \in \mathbb{R}^n$ and analyze how their magnitudes are shared across various subsets, which we term *coalitions* following the terminology of cooperative game theory. A coalition $S \subseteq [m]$, where $[m] := \{1, 2, \dots, m\}$ denotes the index set of all m signals, represents a subset of signals whose collective behavior we wish to quantify. The singleton coalition $\{j\}$ captures behavior unique to signal j , the pair coalition $\{i, j\}$ captures behavior common to signals i and j but potentially shared with others, and the grand coalition $[m]$ captures behavior common to all signals simultaneously. The multistate intersection measures developed below assign a non-negative magnitude to each coalition, decomposing each signal's total norm into contributions from the various coalitions to which it belongs.

4.1 Multistate Embedding with Explicit Neutral State

We now specialize the multistate, norm-preserving embedding from Definition 3.18 to the case where one state is treated as explicitly neutral for coalition analysis. Consider a partition of the real line into K measurable, pairwise disjoint sets

$$\mathcal{B} = \{B_0, B_1, \dots, B_{K-1}\}, \quad (55)$$

where the indexing begins at zero to emphasize the distinguished role of B_0 as a neutral or baseline state. In applications, B_0 might represent values near zero, a reference regime, or any region regarded as qualitatively different from the remaining states. The sets B_1, \dots, B_{K-1} then partition the complement of B_0 according to application requirements. For instance, in financial applications we might define B_1 and B_2 to represent large and small losses, while B_3 and B_4 represent small and large gains. The key feature of this construction is that all magnitudes, including those in the neutral state, are retained explicitly rather than being discarded.

Given such a partition \mathcal{B} , we simply apply the multistate embedding $\psi^{(K)}$ of Definition 3.18 to any signal $A = (A_1, \dots, A_n) \in \mathbb{R}^n$:

$$[\psi^{(K)}(A)]_{i,k} = |A_i| \cdot \mathbf{1}\{A_i \in B_k\}, \quad i = 1, \dots, n, \quad k = 0, \dots, K-1, \quad (56)$$

where $\mathbf{1}\{\cdot\}$ denotes the indicator function. No new embedding is introduced; we simply use $\psi^{(K)}$ with a partition that includes an explicit neutral state B_0 .

Because $\{B_k\}_{k=0}^{K-1}$ forms a partition of \mathbb{R} , each coordinate A_i belongs to exactly one state B_k and therefore contributes its magnitude to exactly one column of the embedded matrix. If $A_i \neq 0$ there is a unique nonzero entry in row i , located in the column corresponding to the state containing A_i , with value $|A_i|$; if $A_i = 0$ the entire row is zero. Summing over states at each coordinate returns $|A_i|$, and summing these across all coordinates yields the

original L^1 norm:

$$\|A\|_1 = \sum_{i=1}^n |A_i| = \sum_{i=1}^n \sum_{k=0}^{K-1} [\psi^{(K)}(A)]_{i,k} = \|\psi^{(K)}(A)\|_1. \quad (57)$$

Thus the multistate embedding $\psi^{(K)}$ preserves the full L^1 norm of the signal while recording how each unit of magnitude is allocated across the qualitative states B_0, \dots, B_{K-1} , including the neutral state.

4.2 Coalition Structure and Intersection Measures

Having embedded each signal into a multistate representation that preserves total magnitude, we now define measures that quantify how magnitude is shared across coalitions of signals. Consider m signals $A_1, \dots, A_m \in \mathbb{R}^n$ and their embeddings $\psi^{(K)}(A_1), \dots, \psi^{(K)}(A_m)$, each represented as an $n \times K$ matrix. A coalition $S \subseteq [m]$ is a nonempty subset of signal indices, representing a group of signals whose collective behavior we wish to analyze. The power set of $[m]$ contains $2^m - 1$ nonempty coalitions, ranging from m singleton coalitions $\{1\}, \{2\}, \dots, \{m\}$ through $\binom{m}{2}$ pairs and larger groups, up to the grand coalition $[m]$ containing all signals.

The fundamental quantity we compute for each coalition is the magnitude that all coalition members share simultaneously while occupying the same state. This requires examining each state channel separately: at coordinate i and state k , we take the minimum embedded value across all signals in coalition S , representing the largest magnitude that all members simultaneously contribute to that state-coordinate combination. Summing these minima across all coordinates and all states yields the total shared magnitude.

Definition 4.1 (Cumulative multistate intersection). For signals $A_1, \dots, A_m \in \mathbb{R}^n$ and a nonempty coalition $S \subseteq [m]$, the cumulative intersection is defined as

$$N(S) := \sum_{k=0}^{K-1} \sum_{i=1}^n \min_{j \in S} \{ [\psi^{(K)}(A_j)]_{i,k} \}. \quad (58)$$

This quantity aggregates the coordinatewise minimum within each state channel, summing over all channels to produce a total shared magnitude measured in the same units as the original signals.

The structure of this definition merits careful examination. The innermost operation, $\min_{j \in S} \{ [\psi^{(K)}(A_j)]_{i,k} \}$, identifies the smallest magnitude contributed by any signal in coalition S to the specific combination of coordinate i and state k . Since each signal contributes magnitude to at most one state at each coordinate (and to exactly one state whenever the underlying coordinate value is nonzero), this minimum is typically zero except when all coalition members happen to assign coordinate i to the same state k . When such agreement occurs, the minimum captures the magnitude that all members can simultaneously contribute. The middle sum over $i = 1, \dots, n$ aggregates these shared contributions across all coordinates, and the outer sum over $k = 0, \dots, K - 1$ combines contributions from all state channels. The resulting scalar $N(S)$ represents the total magnitude that coalition S shares with unanimous state agreement.

An important property of cumulative intersections is their monotonicity with respect to coalition inclusion. If $S \subseteq T$, then $N(T) \leq N(S)$, because taking the minimum over a larger set of signals cannot increase the result. In particular, the grand coalition $[m]$ achieves the smallest cumulative intersection, representing only the magnitude where all m signals simultaneously agree on both coordinate and state. This monotonicity has an important implication: cumulative intersections count shared magnitude with multiplicity. Consider a three-signal example where signals A_1 and A_2 share substantial magnitude, and signals A_2 and A_3 also share substantial magnitude, but the overlap between all three is small. The pairwise cumulative intersections $N(\{1, 2\})$ and $N(\{2, 3\})$ both include the small three-way overlap in their totals, leading to double-counting if we simply sum cumulative intersections to allocate budgets.

To obtain non-overlapping contributions that partition each signal's magnitude exactly, we apply the principle of inclusion–exclusion through Möbius inversion on the Boolean lattice of coalitions. This mathematical technique, fundamental in combinatorics and lattice theory, transforms cumulative counts into exclusive counts by alternately adding and subtracting intersections of nested coalitions.

Definition 4.2 (Exclusive multistate intersection). For a nonempty coalition $S \subseteq [m]$, the exclusive intersection is obtained by Möbius inversion of the cumulative intersections:

$$\widetilde{N}(S) := \sum_{T \supseteq S} \mu(S, T) N(T), \quad (59)$$

where the Möbius function on the Boolean lattice is given by $\mu(S, T) = (-1)^{|T|-|S|}$ for $S \subseteq T$ and $\mu(S, T) = 0$ otherwise.

The Möbius inversion formula assigns to each coalition S the magnitude that is shared by all members of S but not by any larger coalition. For instance, $\widetilde{N}(\{1, 2\})$ represents magnitude shared by signals A_1 and A_2 that is not also shared by any third signal, while $\widetilde{N}(\{1, 2, 3\})$ captures magnitude shared by all three signals simultaneously. The alternating signs in $\mu(S, T) = (-1)^{|T|-|S|}$ implement inclusion–exclusion: we start with the cumulative intersection of S , subtract the cumulative intersections of all coalitions that properly contain S (correcting for over-counting), add back terms that were subtracted too many times, and so forth. Standard properties of Möbius inversion on the Boolean lattice guarantee an exact budget decomposition, and in our min-based, nonnegative construction the resulting exclusive intersections can be interpreted as nonnegative “mass layers” assigned to each coalition.

Remark 4.3 (Computational feasibility of coalition analysis). We note that computing the exclusive intersection $\widetilde{N}(S)$ for all $2^m - 1$ nonempty coalitions is computationally exponential in m , scaling as $\mathcal{O}(2^m n K)$ for the full decomposition. This exhaustive attribution, while theoretically complete, is often not the practical goal. For many applications, analysis is focused on low-order intersections—such as pairwise $\widetilde{N}(\{i, j\})$ and three-way $\widetilde{N}(\{i, j, k\})$ budgets—which remain computationally tractable as m grows. For high-order approximations when m is large, sampling-based methods analogous to Shapley value estimation present a viable path for future investigation.

Proposition 4.4 (Budget identity for exclusive intersections). *For each signal A_j with $j \in [m]$, the L^1 norm decomposes exactly as a sum of exclusive intersections over all coalitions containing j :*

$$\|A_j\|_1 = \sum_{S \ni j} \widetilde{N}(S). \quad (60)$$

Furthermore, in our min-based construction one can show that each $\widetilde{N}(S)$ is nonnegative, so the family $\{\widetilde{N}(S)\}_{S \subseteq [m]}$ forms a bona fide budget allocation rather than involving artificial cancellations.

Remark 4.5 (Intuition for non-negativity). Each cumulative intersection $N(S)$ is built from minima of nonnegative embedded magnitudes. At every coordinate-state pair (i, k) , one can think of each signal as contributing a nonnegative “stack of mass”, and $\min_{j \in S}$ picks out the height that all members of S share. Möbius inversion then peels these shared stacks into layers that are assigned to different coalitions. Because no negative mass is ever introduced at the coordinate level, the resulting exclusive intersections $\widetilde{N}(S)$ can be viewed as nonnegative mass assigned to coalition S . A fully formal derivation is not required for the applications here; the key point is that the decomposition is both lossless and interpretable.

Remark 4.6 (Partitions as modelling choices, not arbitrary binning). Throughout this work, the multistate partition $\mathcal{B} = \{B_0, \dots, B_{K-1}\}$ is not a generic “binning” device but a *modelling choice* that encodes the scientific question of interest. Each state is chosen to represent a qualitatively meaningful regime (e.g. small vs. large gains, mild vs. extreme temperature, baseline vs. elevated insulin use), and the peak-to-peak measures then quantify how mass is allocated across these regimes.

Consequently, the dependence of d_{peak} on the partition should be interpreted in the same way that dependence on a model class is interpreted in classical statistics: different questions call for different state resolutions. Coarser partitions answer high-level questions (“did we move from low to high volatility?”) while finer partitions resolve more detailed hypotheses (“did mass shift specifically from small losses to large gains?”). The framework is therefore *hypothesis-driven* rather than discretization-driven: changing the partition corresponds to changing the question, not to arbitrary numerical binning.

From a technical perspective, working with a state partition is also what enables the budget identities. Once a signal is represented as nonnegative mass over disjoint coordinate-state atoms (i, k) , we can apply the Tanimoto/Jaccard construction on the multistate embedding to obtain a bounded metric and a positive-semidefinite kernel, and perform exact magnitude budgeting across coalitions of signals via Möbius inversion. If one were to skip this state layer and work directly with raw values, it would no longer be possible to decompose each signal’s total magnitude $\|A_j\|_1$ into nonnegative coalition budgets that sum exactly back to $\|A_j\|_1$.

4.3 Illustrative Example: Five-State Partition with Three Signals

To make these abstract definitions concrete, consider three financial return signals analyzed with a five-state partition (one neutral and four non-neutral). We use a symmetric partition around zero with a narrow neutral band and a secondary threshold to distinguish moderate

from extreme movements. The partition (indexed $k = 0, \dots, 4$ so $K = 5$ total states) is:

$$\begin{aligned}
B_0 &= [-0.1, 0.1] && \text{(neutral: negligible movement),} \\
B_1 &= (-\infty, -2.0] && \text{(large loss),} \\
B_2 &= (-2.0, -0.1) && \text{(small loss),} \\
B_3 &= (0.1, 2.0] && \text{(small gain),} \\
B_4 &= (2.0, \infty) && \text{(large gain).}
\end{aligned} \tag{61}$$

This partition creates a symmetric structure around the neutral band, with nested thresholds that separate minor fluctuations from more substantial movements and further distinguish substantial movements from extreme events.

Consider three return signals, each with four temporal observations:

$$A_1 = (8.2, 0.3, -0.05, -5.1), \quad A_2 = (3.1, 0.18, -2.6, -0.07), \quad A_3 = (2.2, 0.0, -1.4, -3.0). \tag{62}$$

These signals exhibit heterogeneous behavior across coordinates: substantial gains at coordinate $i = 1$, modest gains at coordinate $i = 2$, values near zero at coordinate $i = 3$, and substantial losses at coordinate $i = 4$. We now determine the state assignment for each component and construct the embeddings.

State assignments by coordinate. At coordinate $i = 1$, all three signals report positive returns. Signal A_1 has $A_{1,1} = 8.2 > 2.0$, placing it in state B_4 (large gain). Signal A_2 has $A_{2,1} = 3.1 > 2.0$, also in B_4 . Signal A_3 has $A_{3,1} = 2.2 > 2.0$, again in B_4 . All three signals therefore contribute to the large-gain state at this coordinate, with respective magnitudes 8.2, 3.1, and 2.2.

At coordinate $i = 2$, we observe smaller positive values. Signal A_1 has $A_{1,2} = 0.3$, which satisfies $0.1 < 0.3 \leq 2.0$ and therefore belongs to B_3 (small gain) with magnitude 0.3. Signal A_2 has $A_{2,2} = 0.18 \in (0.1, 2.0]$, also in B_3 with magnitude 0.18. Signal A_3 has $A_{3,2} = 0.0$, which lies in $[-0.1, 0.1]$ and therefore enters B_0 (neutral) with magnitude 0.0. Here two signals agree on small gains while the third signal is neutral.

At coordinate $i = 3$, values are negative or near-zero. Signal A_1 has $A_{1,3} = -0.05$, which falls in $[-0.1, 0.1]$ and is assigned to B_0 (neutral) with magnitude 0.05. Signal A_2 has $A_{2,3} = -2.6$, which satisfies $-2.6 \leq -2.0$ and therefore belongs to B_1 (large loss) with magnitude 2.6. Signal A_3 has $A_{3,3} = -1.4 \in (-2.0, -0.1)$, placing it in B_2 (small loss) with magnitude 1.4. All three signals occupy different states at this coordinate, exhibiting no agreement.

At coordinate $i = 4$, substantial losses dominate. Signal A_1 has $A_{1,4} = -5.1 \leq -2.0$, assigning it to B_1 (large loss) with magnitude 5.1. Signal A_2 has $A_{2,4} = -0.07 \in [-0.1, 0.1]$, placing it in B_0 (neutral) with magnitude 0.07. Signal A_3 has $A_{3,4} = -3.0 \leq -2.0$, assigning it to B_1 (large loss) with magnitude 3.0. Signals A_1 and A_3 agree on large losses while A_2 remains neutral.

These state assignments determine the structure of the embedded matrices. For signal A_1 , the embedding $\psi^{(5)}(A_1)$ is a 4×5 matrix (since we have $n = 4$ coordinates and $K = 5$ states, with the neutral state arranged in column 0). Row 1 has its sole nonzero entry 8.2 in column 4 (state B_4). Row 2 has 0.3 in column 3 (state B_3). Row 3 has 0.05 in column 0

(neutral state B_0). Row 4 has 5.1 in column 1 (state B_1). The embeddings for A_2 and A_3 follow analogously from the assignments above.

The L^1 norms, computed by summing the absolute values of all coordinates including those in the neutral state, are

$$\|A_1\|_1 = 8.2 + 0.3 + 0.05 + 5.1 = 13.65, \quad (63)$$

$$\|A_2\|_1 = 3.1 + 0.18 + 2.6 + 0.07 = 5.95, \quad (64)$$

$$\|A_3\|_1 = 2.2 + 0.0 + 1.4 + 3.0 = 6.6. \quad (65)$$

These norms account for every magnitude in each signal, consistent with the norm preservation property in equation (57).

Cumulative intersections for selected coalitions. We now compute cumulative intersections for several coalitions to illustrate equation (58). Consider first the coalition $S = \{1, 2\}$, representing the shared behavior between signals A_1 and A_2 . We evaluate the double sum by examining each state k and each coordinate i , computing $\min\{[\psi^{(5)}(A_1)]_{i,k}, [\psi^{(5)}(A_2)]_{i,k}\}$ and summing the results.

At state B_4 (large gains), only coordinate $i = 1$ has both signals present. The minimum is $\min\{8.2, 3.1\} = 3.1$. At state B_3 (small gains), only coordinate $i = 2$ has both signals present, yielding $\min\{0.3, 0.18\} = 0.18$. At state B_1 (large losses), coordinate $i = 4$ has A_1 contributing 5.1 but A_2 contributing 0 (since A_2 is in the neutral state at $i = 4$), giving minimum 0. At state B_2 (small losses), coordinate $i = 3$ has A_2 contributing 2.6 but A_1 contributing 0 (since A_1 is neutral at $i = 3$), again giving minimum 0. At the neutral state B_0 , coordinates $i = 3$ and $i = 4$ have one or both signals present, but examining the minima: at $i = 3$, $\min\{0.05, 0\} = 0$; at $i = 4$, $\min\{0, 0.07\} = 0$. Summing all nonzero contributions,

$$N(\{1, 2\}) = 3.1 + 0.18 = 3.28. \quad (66)$$

Next consider the grand coalition $S = \{1, 2, 3\}$, requiring agreement among all three signals. At state B_4 and coordinate $i = 1$, all three signals contribute (magnitudes 8.2, 3.1, 2.2), yielding minimum $\min\{8.2, 3.1, 2.2\} = 2.2$. At state B_3 and coordinate $i = 2$, signals A_1 and A_2 contribute (0.3 and 0.18) but A_3 contributes 0 (being in the neutral state), giving minimum 0. At state B_1 , coordinate $i = 4$ has A_1 and A_3 contributing (5.1 and 3.0) but A_2 contributes 0, again minimum 0. At state B_2 , only A_3 contributes at $i = 3$, so the minimum is 0. At the neutral state B_0 , no coordinate has all three signals simultaneously in the neutral state (at $i = 2$, only A_3 is neutral; at $i = 3$, only A_1 is neutral; at $i = 4$, only A_2 is neutral), producing minimum 0 at all neutral-state positions. Therefore,

$$N(\{1, 2, 3\}) = 2.2. \quad (67)$$

Exclusive intersections through Möbius inversion. The exclusive intersection for coalition $\{1, 2\}$ subtracts the cumulative intersection of any coalition properly containing $\{1, 2\}$, which is only $\{1, 2, 3\}$ in this three-signal example. The Möbius function gives $\mu(\{1, 2\}, \{1, 2\}) = (-1)^0 = 1$ and $\mu(\{1, 2\}, \{1, 2, 3\}) = (-1)^1 = -1$, so equation (59) yields

$$\widetilde{N}(\{1, 2\}) = N(\{1, 2\}) - N(\{1, 2, 3\}) = 3.28 - 2.2 = 1.08. \quad (68)$$

This value represents the magnitude that signals A_1 and A_2 share exclusively without participation from A_3 . For the grand coalition, no coalition properly contains $\{1, 2, 3\}$, so

$$\widetilde{N}(\{1, 2, 3\}) = N(\{1, 2, 3\}) = 2.2. \quad (69)$$

Similar calculations for other coalitions (singletons, other pairs, and remaining triples if we had more signals) would produce a complete decomposition satisfying Proposition 4.4. Each signal's norm $\|A_j\|_1$ equals the sum of $\widetilde{N}(S)$ over all coalitions S containing j , providing exact budget accounting.

4.4 Dimensional Reduction: Recovering Two-State Summaries

The five-state partition employed in the preceding example provides detailed information about the distribution of gains and losses, distinguishing large from small movements and tracking neutral behavior separately. However, many applications require coarser summaries that aggregate these fine distinctions into broader categories. A common requirement is a simple two-state view separating negative behavior (losses) from positive behavior (gains), potentially with neutral magnitudes reported separately or allocated according to context-specific rules. This section demonstrates how such dimensional reduction can be achieved through post-intersection aggregation of state channels, avoiding the need to recompute intersections from scratch at the coarser resolution.

Define aggregated state groups by partitioning the state indices. Let $\mathcal{G}_- \subset \{0, 1, \dots, K-1\}$ denote the collection of loss-state indices and \mathcal{G}_+ the collection of gain-state indices. In the five-state example,

$$\mathcal{G}_- := \{1, 2\} \quad (\text{large loss } B_1, \text{ small loss } B_2), \quad \mathcal{G}_+ := \{3, 4\} \quad (\text{small gain } B_3, \text{ large gain } B_4). \quad (70)$$

The neutral state B_0 (index 0) is handled separately, either reported as a third category or omitted from the positive-negative dichotomy depending on application needs. The question now is how to compute cumulative intersections for these aggregated categories without re-embedding signals at a coarser resolution.

A naive approach might suggest taking the minimum across signals after first summing over the states within each group. This approach would compute, for coalition S , the quantity

$$(\text{INCORRECT}) \quad \min_{j \in S} \left\{ \sum_{k \in \mathcal{G}_+} \sum_{i=1}^n [\psi^{(K)}(A_j)]_{i,k} \right\}. \quad (71)$$

This formula first aggregates each signal's positive-state magnitudes across all coordinates, producing a single positive-total for each signal, then takes the minimum across the coalition. However, this sequence of operations can severely overestimate the shared magnitude. Consider two signals that both have substantial positive contributions but at different coordinates: signal A_1 might have large gains at coordinates 1 and 2 but losses at coordinates 3 and 4, while signal A_2 has losses at 1 and 2 but large gains at 3 and 4. Summing each signal's positive magnitudes first would produce large totals for both, and taking the minimum would suggest substantial shared positive behavior even though the signals never simultaneously

exhibit gains at the same coordinate. This aggregation-then-minimum approach violates the coordinate-wise agreement structure that underlies the intersection concept.

The correct approach maintains coordinate-wise resolution throughout the minimum operation, aggregating state channels only after computing per-coordinate, per-state minima. This ensures that we count only magnitude where coalition members agree on both coordinate and directional category.

Proposition 4.7 (Post-intersection state aggregation). *Let $N(S)$ denote the cumulative intersection computed via equation (58) using the fine partition $\mathcal{B} = \{B_0, B_1, \dots, B_{K-1}\}$. Define aggregated two-state cumulative intersections by summing the per-coordinate, per-state minima after the minimum operation:*

$$N_+(S) := \sum_{k \in \mathcal{G}_+} \sum_{i=1}^n \min_{j \in S} \{[\psi^{(K)}(A_j)]_{i,k}\}, \quad N_-(S) := \sum_{k \in \mathcal{G}_-} \sum_{i=1}^n \min_{j \in S} \{[\psi^{(K)}(A_j)]_{i,k}\}. \quad (72)$$

Similarly define the neutral contribution as

$$N_0(S) := \sum_{i=1}^n \min_{j \in S} \{[\psi^{(K)}(A_j)]_{i,0}\}. \quad (73)$$

Then $N_+(S) + N_-(S) + N_0(S) = N(S)$, and no intersection mass is lost, gained, or distorted by this aggregation. Furthermore, the aggregated quantities $N_{\pm}(S)$ can be used to define exclusive intersections via Möbius inversion in the usual way, producing a valid two-state budget decomposition.

Proof. By definition, $N(S) = \sum_{k=0}^{K-1} \sum_{i=1}^n \min_{j \in S} \{[\psi^{(K)}(A_j)]_{i,k}\}$. Partitioning the sum over k into the three groups $\{0\}$ (neutral), \mathcal{G}_- (losses), and \mathcal{G}_+ (gains) yields $N_0(S) + N_-(S) + N_+(S)$ by definition. Since the min operations are performed before any aggregation, the coordinate-wise agreement structure is preserved exactly, and the sum equals the original fine-grained cumulative intersection. Möbius inversion applied to the aggregated cumulative intersections produces valid exclusive intersections because the Boolean lattice structure depends only on coalition containment, not on the state resolution used to compute intersection magnitudes. \square

Remark 4.8 (Order of operations is critical). The proposition emphasizes that state aggregation must occur *after* computing the coordinatewise minima within each state channel. Reversing this order—computing minima after summing states as in equation (71)—produces incorrect results that violate the intersection semantics and can dramatically overestimate shared magnitude. The correct sequence is: (1) compute minima per state and per coordinate, (2) sum over coordinates within each state to get state-specific contributions, (3) aggregate across states as desired. This order respects the fundamental principle that intersection measures quantify simultaneous agreement at each coordinate.

Two-state summary of the numerical example. Applying this aggregation to the computations from Section 4.3, we extract the positive and negative contributions from

coalition $\{1, 2\}$. The only nonzero per-state, per-coordinate minima were 3.1 at state B_4 (large gain) and 0.18 at state B_3 (small gain), both of which belong to \mathcal{G}_+ . Therefore,

$$N_+(\{1, 2\}) = 3.1 + 0.18 = 3.28, \quad N_-(\{1, 2\}) = 0, \quad N_0(\{1, 2\}) = 0, \quad (74)$$

confirming that $N(\{1, 2\}) = 3.28$ arises entirely from shared positive behavior. For the grand coalition $\{1, 2, 3\}$, the only nonzero contribution was 2.2 at state B_4 , yielding

$$N_+(\{1, 2, 3\}) = 2.2, \quad N_-(\{1, 2, 3\}) = 0, \quad N_0(\{1, 2, 3\}) = 0. \quad (75)$$

The two-state exclusive intersections follow immediately by Möbius inversion:

$$\widetilde{N}_+(\{1, 2\}) = N_+(\{1, 2\}) - N_+(\{1, 2, 3\}) = 3.28 - 2.2 = 1.08, \quad \widetilde{N}_+(\{1, 2, 3\}) = 2.2. \quad (76)$$

These values coincide with the full five-state analysis because, in this particular example, all shared magnitude occurred in the positive states. In general, both $N_+(S)$ and $N_-(S)$ would be nonzero, and each would admit its own Möbius-inverted exclusive decomposition.

Summary and interpretation. The multistate framework provides complete magnitude accounting through explicit representation of neutral states, cumulative intersections that quantify overlapping behavior across coalitions, and exclusive intersections that partition each signal’s magnitude into non-overlapping coalition contributions. When finer state resolution is unnecessary, dimensional reduction through post-intersection aggregation recovers coarser summaries without computational redundancy or loss of mathematical structure. This unified treatment enables analysts to work at the natural resolution for their problem while retaining the flexibility to produce summaries at multiple scales from a single set of calculations.

4.5 Probabilistic Interpretation via Normalized Embeddings

The multistate embedding framework developed in the preceding sections admits a natural probabilistic interpretation that connects our geometric similarity measures to classical concepts from probability theory and information theory. This connection provides both theoretical insight—revealing that our distance measures are monotone transformations of total variation distance—and practical utility, as it enables the application of probabilistic reasoning and data-processing inequalities to analyze the behavior of similarity measures under partition refinement or coarsening.

The key observation is that the embedding $\psi^{(K)}(A)$ assigns a non-negative magnitude to each combination of coordinate index $i \in \{1, \dots, n\}$ and state index $k \in \{0, \dots, K-1\}$, producing what amounts to a discrete distribution of magnitude across the Cartesian product of coordinates and states. When we normalize by the signal’s total L^1 norm, this distribution becomes a probability distribution, with the probability mass at each coordinate-state pair proportional to the magnitude that coordinate contributes when occupying that particular state. Comparing two signals then reduces to comparing two probability distributions over the same discrete space, enabling us to invoke the rich theory of probability metrics.

4.5.1 Construction of the probability space

We formalize the probabilistic structure by defining an appropriate sample space and measure. Let $\mathcal{B} = \{B_0, \dots, B_{K-1}\}$ denote a measurable partition of \mathbb{R} as in Section 4.1, and let $\psi^{(K)}$ be the multistate embedding mapping signals $A \in \mathbb{R}^n$ to matrices in $\mathbb{R}_{\geq 0}^{n \times K}$. We construct a finite sample space whose elements represent the possible combinations of coordinate position and state membership.

Definition 4.9 (Sample space of coordinate-state pairs). The sample space of coordinate-state pairs, which we call *atoms* in the sense of atomic probability theory (indivisible elementary events), is defined as the Cartesian product

$$\Omega := \{1, \dots, n\} \times \{0, \dots, K-1\}. \quad (77)$$

Each element $\omega = (i, k) \in \Omega$ represents the event that we observe coordinate i while it occupies state k . The σ -algebra on Ω is taken to be the full power set $\mathcal{F} := 2^\Omega$, which is the natural choice for finite spaces and ensures that all subsets are measurable. The space (Ω, \mathcal{F}) thus has exactly $n \cdot K$ atoms, one for each coordinate-state combination.

The terminology "atom" deserves clarification. In measure theory, an atom is a measurable set of positive measure that cannot be decomposed into smaller measurable sets of positive measure. For finite discrete spaces like Ω , each singleton $\{(i, k)\}$ is an atom, and the entire space is a countable (in this case finite) union of such atoms. This atomic structure means that probability distributions on (Ω, \mathcal{F}) are completely determined by specifying the probability mass assigned to each of the $n \cdot K$ elementary events, with no continuous components or finer internal structure to consider.

For any signal $A \in \mathbb{R}^n$, the multistate embedding $\psi^{(K)}$ naturally induces a finite measure on this space by assigning to each atom the magnitude that A contributes to the corresponding coordinate-state combination.

Definition 4.10 (Magnitude measure induced by a signal). For a signal $A \in \mathbb{R}^n$, define the finite measure ν_A on the measurable space (Ω, \mathcal{F}) by specifying its value on each atom:

$$\nu_A(\{(i, k)\}) := [\psi^{(K)}(A)]_{i,k} = |A_i| \cdot \mathbf{1}\{A_i \in B_k\}. \quad (78)$$

For arbitrary measurable sets $E \in \mathcal{F}$, extend by countable additivity: $\nu_A(E) = \sum_{\omega \in E} \nu_A(\{\omega\})$. The total measure of the space is

$$\nu_A(\Omega) = \sum_{i=1}^n \sum_{k=0}^{K-1} \nu_A(\{(i, k)\}) = \|A\|_1, \quad (79)$$

which follows from equation (57).

The measure ν_A assigns mass to exactly one atom for each coordinate i , so at most n atoms carry positive (nonzero) mass. If $A_i = 0$ for some i , the corresponding atom has zero mass. When the signal A is nonzero, meaning $\|A\|_1 > 0$, we can normalize ν_A to produce a probability measure.

Definition 4.11 (Normalized probability distribution). For a nonzero signal $A \in \mathbb{R}^n$ with $\|A\|_1 > 0$, define the probability measure P_A on (Ω, \mathcal{F}) by normalization:

$$P_A := \frac{\nu_A}{\|A\|_1}. \quad (80)$$

Explicitly, for each atom $(i, k) \in \Omega$,

$$P_A(\{(i, k)\}) = \frac{[\psi(K)(A)]_{i,k}}{\|A\|_1} = \frac{|A_i| \cdot \mathbf{1}\{A_i \in B_k\}}{\|A\|_1}. \quad (81)$$

This defines a probability distribution over coordinate-state pairs, where the probability of atom (i, k) equals the fraction of signal A 's total magnitude contributed by coordinate i when it occupies state k .

For zero signals with $\|A\|_1 = 0$, normalization is undefined, so the probabilistic interpretation is restricted to nonzero signals. In practice, these degenerate cases are handled directly at the level of the original similarity: if both signals are identically zero (or lie entirely within the tolerance band), we treat them as perfectly similar, while if exactly one signal carries nonzero magnitude, the peak-to-peak similarity reduces to the classical Jaccard-style comparison between an empty and a nonempty object. These edge cases lie on the boundary of the domain where $\|A\|_1 > 0$ and do not affect the probabilistic formulation for nonzero signals.

4.5.2 Connection to total variation distance

With the probabilistic framework in place, we now make precise the relationship between the peak-to-peak similarity J_{peak} (and its associated distance d_{peak}) and the total variation distance between the finite measures induced by two signals. The key point is that the original $J_{\text{peak}}(A, B)$ is defined on *unnormalized* magnitude measures and therefore depends both on the *shape* and the *total mass* (L^1 norm) of the signals. The total variation distance must therefore be taken between the corresponding finite measures, rather than solely between the normalized probability distributions.

Recall from Definition 4.10 that each signal $A \in \mathbb{R}^n$ induces a finite measure ν_A on (Ω, \mathcal{F}) via the multistate embedding $\psi^{(K)}$, with total mass

$$M_A := \nu_A(\Omega) = \|A\|_1, \quad (82)$$

and analogously $M_B := \nu_B(\Omega) = \|B\|_1$ for signal B . The total variation distance between the finite measures ν_A and ν_B is defined by

$$\text{TV}(\nu_A, \nu_B) := \frac{1}{2} \sum_{\omega \in \Omega} |\nu_A(\{\omega\}) - \nu_B(\{\omega\})|. \quad (83)$$

Proposition 4.12 (Peak-to-peak distance as a transform of total variation). *Let $A, B \in \mathbb{R}^n$ and let ν_A, ν_B be the finite measures on (Ω, \mathcal{F}) induced by their multistate embeddings as in Definition 4.10. Denote*

$$M_A := \nu_A(\Omega) = \|A\|_1, \quad M_B := \nu_B(\Omega) = \|B\|_1, \quad (84)$$

and let

$$\text{TV}(\nu_A, \nu_B) := \frac{1}{2} \sum_{\omega \in \Omega} |\nu_A(\{\omega\}) - \nu_B(\{\omega\})| \quad (85)$$

be their total variation distance as finite measures. Then the peak-to-peak similarity and distance satisfy

$$J_{\text{peak}}(A, B) = \frac{M_A + M_B - 2 \text{TV}(\nu_A, \nu_B)}{M_A + M_B + 2 \text{TV}(\nu_A, \nu_B)}, \quad (86)$$

and consequently

$$d_{\text{peak}}(A, B) = 1 - J_{\text{peak}}(A, B) = \frac{4 \text{TV}(\nu_A, \nu_B)}{M_A + M_B + 2 \text{TV}(\nu_A, \nu_B)}. \quad (87)$$

Equivalently, if we define the normalized discrepancy

$$\delta(A, B) := \frac{\text{TV}(\nu_A, \nu_B)}{\frac{1}{2}(M_A + M_B)} \in [0, 1], \quad (88)$$

then

$$J_{\text{peak}}(A, B) = \frac{1 - \delta(A, B)}{1 + \delta(A, B)}, \quad d_{\text{peak}}(A, B) = \frac{2 \delta(A, B)}{1 + \delta(A, B)}. \quad (89)$$

Proof. Write

$$x_\omega := \nu_A(\{\omega\}), \quad y_\omega := \nu_B(\{\omega\}), \quad (90)$$

so that $x_\omega, y_\omega \geq 0$ for all $\omega \in \Omega$ and $\sum_\omega x_\omega = M_A$, $\sum_\omega y_\omega = M_B$. By Definition 4.10, together with the multistate embedding $\psi^{(K)}$, the peak-to-peak similarity is

$$J_{\text{peak}}(A, B) = \frac{\sum_{\omega \in \Omega} \min\{x_\omega, y_\omega\}}{\sum_{\omega \in \Omega} \max\{x_\omega, y_\omega\}}. \quad (91)$$

At each atom $\omega \in \Omega$ we have the pointwise identities

$$\max\{x_\omega, y_\omega\} + \min\{x_\omega, y_\omega\} = x_\omega + y_\omega, \quad (92)$$

$$\max\{x_\omega, y_\omega\} - \min\{x_\omega, y_\omega\} = |x_\omega - y_\omega|. \quad (93)$$

Summing over all ω gives

$$\sum_{\omega} \max\{x_\omega, y_\omega\} + \sum_{\omega} \min\{x_\omega, y_\omega\} = \sum_{\omega} x_\omega + \sum_{\omega} y_\omega = M_A + M_B, \quad (94)$$

$$\sum_{\omega} \max\{x_\omega, y_\omega\} - \sum_{\omega} \min\{x_\omega, y_\omega\} = \sum_{\omega} |x_\omega - y_\omega| = 2 \text{TV}(\nu_A, \nu_B). \quad (95)$$

Let

$$S_{\max} := \sum_{\omega} \max\{x_\omega, y_\omega\}, \quad S_{\min} := \sum_{\omega} \min\{x_\omega, y_\omega\}. \quad (96)$$

Equations (94)–(95) form a linear system:

$$S_{\max} + S_{\min} = M_A + M_B, \quad S_{\max} - S_{\min} = 2 \text{TV}(\nu_A, \nu_B). \quad (97)$$

Solving,

$$S_{\max} = \frac{(M_A + M_B) + 2 \operatorname{TV}(\nu_A, \nu_B)}{2}, \quad (98)$$

$$S_{\min} = \frac{(M_A + M_B) - 2 \operatorname{TV}(\nu_A, \nu_B)}{2}. \quad (99)$$

Substituting into $J_{\text{peak}} = S_{\min}/S_{\max}$ yields

$$J_{\text{peak}}(A, B) = \frac{M_A + M_B - 2 \operatorname{TV}(\nu_A, \nu_B)}{M_A + M_B + 2 \operatorname{TV}(\nu_A, \nu_B)}, \quad (100)$$

which is (86). The distance formula (87) follows by computing $1 - J_{\text{peak}}$ and simplifying.

For the normalized discrepancy, note that

$$\delta(A, B) = \frac{\operatorname{TV}(\nu_A, \nu_B)}{\frac{1}{2}(M_A + M_B)} = \frac{2 \operatorname{TV}(\nu_A, \nu_B)}{M_A + M_B}, \quad (101)$$

so substituting $\operatorname{TV}(\nu_A, \nu_B) = \frac{1}{2}(M_A + M_B) \delta(A, B)$ into (86) gives

$$J_{\text{peak}}(A, B) = \frac{1 - \delta(A, B)}{1 + \delta(A, B)}, \quad (102)$$

and hence

$$d_{\text{peak}}(A, B) = 1 - J_{\text{peak}}(A, B) = \frac{2 \delta(A, B)}{1 + \delta(A, B)}. \quad (103)$$

This completes the proof. \square

The representation (89) shows that d_{peak} is a strictly increasing function of the normalized discrepancy $\delta(A, B)$: the map $t \mapsto \frac{2t}{1+t}$ has derivative

$$\frac{d}{dt} \left(\frac{2t}{1+t} \right) = \frac{2}{(1+t)^2} > 0 \quad \text{for } t \in [0, 1], \quad (104)$$

so larger total variation (relative to average mass) corresponds to larger peak-to-peak distance.

Remark 4.13 (Probability-normalized special case). When the signals have equal L^1 norm, $M_A = M_B > 0$, the finite measures ν_A and ν_B can be written as scaled versions of the probability measures P_A and P_B of Definition 4.11:

$$\nu_A = M_A P_A, \quad \nu_B = M_A P_B. \quad (105)$$

In this case,

$$\operatorname{TV}(\nu_A, \nu_B) = M_A \operatorname{TV}(P_A, P_B), \quad \frac{1}{2}(M_A + M_B) = M_A, \quad (106)$$

and hence $\delta(A, B) = \operatorname{TV}(P_A, P_B)$. The formulas (89) reduce to

$$J_{\text{peak}}(A, B) = \frac{1 - \operatorname{TV}(P_A, P_B)}{1 + \operatorname{TV}(P_A, P_B)}, \quad d_{\text{peak}}(A, B) = \frac{2 \operatorname{TV}(P_A, P_B)}{1 + \operatorname{TV}(P_A, P_B)}. \quad (107)$$

Thus, when signals are compared after L^1 -normalization (or naturally have equal total magnitude), the peak-to-peak distance becomes a simple monotone transform of the usual total variation distance between the induced probability distributions P_A and P_B on the coordinate-state space (Ω, \mathcal{F}) .

Remark 4.14 (Ordinal Transport vs. Modular Budgeting). The multistate partitions $\mathcal{B} = \{B_0, \dots, B_{K-1}\}$ employed in this work (e.g., Eq. (55)) often possess a natural ordinal structure. Consequently, one could define a cumulative magnitude distribution F_A for a signal A by summing the induced measure ν_A (Def. 4.10) over ordered states:

$$F_A(k) = \sum_{j=0}^k \nu_A(\{(i, B_j) \mid i \in \{1, \dots, n\}\}), \quad k = 0, \dots, K-1.$$

Constructing distances based on F_A —effectively moving from a PDF-like view to a CDF-like view—would shift the geometric framework from Jaccard/Total Variation to the Wasserstein (W_1) or Kolmogorov–Smirnov family.

We explicitly avoid this construction to preserve two structural properties essential to the proposed framework. First, the binwise Jaccard geometry adheres to an “exact-match” philosophy: the similarity between a *Large Loss* and a *Large Gain* is zero, independent of their ordinal separation. While a transport-based (CDF) metric would penalize this disagreement more heavily than a *Large Loss/Small Loss* discrepancy, it introduces gradient sensitivity at the cost of strictly modular accounting. Second, and most critically, the binwise independence of $\psi^{(K)}$ ensures that the space of coalitions forms a Boolean lattice with independent atoms. This independence is the algebraic prerequisite for the exact Möbius budget decomposition derived in Section 4.4. Cumulative dependencies would couple the states, breaking the lattice structure required for additive coalition budgeting.

4.5.3 Data processing inequality and coarsening

The probabilistic interpretation in Section 4.5.1 allows us to view each signal A as inducing a finite measure ν_A on the coordinate–state space $\Omega = \{1, \dots, n\} \times \{0, \dots, K-1\}$. On a finite state space, the total variation distance between two finite measures ν_A and ν_B takes the standard discrete form

$$\text{TV}(\nu_A, \nu_B) = \frac{1}{2} \sum_{\omega \in \Omega} |\nu_A(\{\omega\}) - \nu_B(\{\omega\})|,$$

see, for example, Levin, Peres, and Wilmer (Levin et al., 2017, Ch. 4.1). This representation makes it transparent that *coarsening* the underlying partition—by merging atoms of Ω into larger categories—can only decrease total variation. The next lemma records the corresponding monotonicity property for the peak-to-peak distance.

Lemma 4.15 (Monotonicity under partition coarsening). *Let $\pi : \Omega \rightarrow \Omega'$ be a measurable mapping that coarsens the atom structure, meaning that π maps multiple atoms in Ω to single atoms in Ω' , effectively merging coordinate–state categories. For example, π might map both (i, B_1) (large loss) and (i, B_2) (small loss) to a single atom (i, loss) in a coarser partition.*

Let ν_A, ν_B be the finite measures induced by signals A, B on (Ω, \mathcal{F}) as in Definition 4.10, and define their pushforward measures on (Ω', \mathcal{F}') by

$$\nu'_A := \nu_A \circ \pi^{-1}, \quad \nu'_B := \nu_B \circ \pi^{-1}. \quad (108)$$

Then

$$\text{TV}(\nu'_A, \nu'_B) \leq \text{TV}(\nu_A, \nu_B), \quad (109)$$

and consequently, if $d'_{\text{peak}}(A, B)$ denotes the peak-to-peak distance computed using the coarsened partition,

$$d'_{\text{peak}}(A, B) \leq d_{\text{peak}}(A, B). \quad (110)$$

That is, coarsening the state partition can only decrease the measured distance (or equivalently, increase the measured similarity).

Proof. On the finite space Ω , total variation admits the discrete representation

$$\text{TV}(\nu_A, \nu_B) = \frac{1}{2} \sum_{\omega \in \Omega} |\nu_A(\{\omega\}) - \nu_B(\{\omega\})|.$$

Under the coarsening map π , each coarse atom $\omega' \in \Omega'$ collects the mass of its preimage $\pi^{-1}(\{\omega'\}) \subseteq \Omega$, so

$$\nu'_A(\{\omega'\}) = \sum_{\omega \in \pi^{-1}(\{\omega'\})} \nu_A(\{\omega\}), \quad \nu'_B(\{\omega'\}) = \sum_{\omega \in \pi^{-1}(\{\omega'\})} \nu_B(\{\omega\}).$$

Applying the triangle inequality inside each preimage and summing over $\omega' \in \Omega'$ shows that merging atoms can only decrease the total variation, yielding the contraction property

$$\text{TV}(\nu'_A, \nu'_B) \leq \text{TV}(\nu_A, \nu_B). \quad (111)$$

Let $M_A = \nu_A(\Omega)$ and $M_B = \nu_B(\Omega)$ be the total masses. Since π merely merges atoms, the pushforward measures preserve total mass:

$$\nu'_A(\Omega') = \nu_A(\Omega) = M_A, \quad \nu'_B(\Omega') = \nu_B(\Omega) = M_B. \quad (112)$$

Define the normalized discrepancies as in (88):

$$\delta(A, B) := \frac{\text{TV}(\nu_A, \nu_B)}{\frac{1}{2}(M_A + M_B)}, \quad \delta'(A, B) := \frac{\text{TV}(\nu'_A, \nu'_B)}{\frac{1}{2}(M_A + M_B)}. \quad (113)$$

The contraction inequality implies

$$\delta'(A, B) \leq \delta(A, B). \quad (114)$$

By Proposition 4.12, the peak-to-peak distances are given by

$$d_{\text{peak}}(A, B) = \frac{2\delta(A, B)}{1 + \delta(A, B)}, \quad d'_{\text{peak}}(A, B) = \frac{2\delta'(A, B)}{1 + \delta'(A, B)}, \quad (115)$$

cf. equation (89). The function $f(t) = \frac{2t}{1+t}$ is strictly increasing on $[0, 1]$, since $f'(t) = \frac{2}{(1+t)^2} > 0$, and therefore

$$\delta'(A, B) \leq \delta(A, B) \implies d'_{\text{peak}}(A, B) \leq d_{\text{peak}}(A, B). \quad (116)$$

□

Remark 4.16 (Refinement increases distance, coarsening decreases distance). Lemma 4.15 has an important converse implication. While coarsening partitions decreases distance (and increases similarity), refining partitions—splitting existing states into finer subcategories—can only increase the total variation distance and therefore increase d_{peak} while decreasing J_{peak} . This monotonicity property provides theoretical justification for the post-intersection aggregation procedure advocated in Proposition 4.7. When we aggregate state contributions *after* computing coordinatewise minima, we are effectively computing the distance at the fine resolution and then reporting aggregated statistics, which preserves the fine-scale distinction. By contrast, coarsening *before* computing intersections would compute a fundamentally smaller distance corresponding to the coarser partition. The choice of partition granularity thus directly controls the sensitivity of the similarity measure: finer partitions detect more subtle differences in signal behavior, while coarser partitions focus on broader patterns and intentionally discard fine detail.

Remark 4.17 (Zero L^1 mass as a physical vacuum). As in Remark 3.1, the case $\|A\|_1 = \|B\|_1 = 0$ corresponds to the unique “vacuum” state with no mass at any coordinate. In particular, two zero-mass signals represent the same physical regime, and the peak-to-peak similarity assigns $J_{\text{peak}}(0, 0) = 1$ and $d_{\text{peak}}(0, 0) = 0$. This boundary case lies outside the normalized-discrepancy formula (88), which assumes $M_A + M_B > 0$, but is fully consistent with the total-variation representation $TV(\nu_A, \nu_B) = 0$ when $\nu_A = \nu_B = 0$.

4.5.4 Numerical verification of the total variation relationship

To make the abstract connection between peak-to-peak measures and total variation concrete, we work through a simple numerical example demonstrating that both computational routes—direct min–max calculation versus the total-variation formulation—yield identical results.

Example 4.18 (Verification of the TV relationship for J_{peak}). Consider signals with $n = 3$ coordinates and a three-state partition ($K = 3$) defined by

$$B_0 = [-0.1, 0.1] \text{ (neutral)}, \quad B_1 = (0.1, \infty) \text{ (positive)}, \quad B_2 = (-\infty, -0.1) \text{ (negative)}. \quad (117)$$

Let the two signals be

$$A = (2.0, 0.3, -1.1), \quad B = (1.6, 0.0, -0.4). \quad (118)$$

We compute the peak-to-peak similarity and distance through two independent routes.

State assignments and norms. For signal A : coordinate $A_1 = 2.0 > 0.1$ belongs to state B_1 with magnitude 2.0; coordinate $A_2 = 0.3 \in (0.1, \infty)$ belongs to state B_1 with magnitude 0.3; coordinate $A_3 = -1.1 < -0.1$ belongs to state B_2 with magnitude 1.1. Thus

$$\|A\|_1 = 2.0 + 0.3 + 1.1 = 3.4. \quad (119)$$

For signal B : coordinate $B_1 = 1.6 > 0.1$ belongs to B_1 with magnitude 1.6; coordinate $B_2 = 0.0 \in [-0.1, 0.1]$ belongs to B_0 with magnitude 0.0; coordinate $B_3 = -0.4 < -0.1$ belongs to B_2 with magnitude 0.4. Hence

$$\|B\|_1 = 1.6 + 0.0 + 0.4 = 2.0. \quad (120)$$

At the level of the magnitude measures ν_A, ν_B on $\Omega = \{1, 2, 3\} \times \{0, 1, 2\}$, the only atoms with nonzero mass are

$$(1, B_1), (2, B_1), (3, B_2), \quad (121)$$

with

$$\nu_A = (2.0, 0.3, 1.1), \quad \nu_B = (1.6, 0.0, 0.4) \quad (122)$$

in that order.

Route 1: Direct min–max computation. At each atom, compute the minimum and maximum magnitudes:

- At $(1, B_1)$: $\min\{2.0, 1.6\} = 1.6$, $\max\{2.0, 1.6\} = 2.0$.
- At $(2, B_1)$: $\min\{0.3, 0.0\} = 0.0$, $\max\{0.3, 0.0\} = 0.3$.
- At $(3, B_2)$: $\min\{1.1, 0.4\} = 0.4$, $\max\{1.1, 0.4\} = 1.1$.

Summing across all atoms gives

$$\sum_{\omega \in \Omega} \min\{\nu_A(\omega), \nu_B(\omega)\} = 1.6 + 0.0 + 0.4 = 2.0, \quad (123)$$

$$\sum_{\omega \in \Omega} \max\{\nu_A(\omega), \nu_B(\omega)\} = 2.0 + 0.3 + 1.1 = 3.4. \quad (124)$$

Therefore the peak-to-peak similarity and distance are

$$J_{\text{peak}}(A, B) = \frac{2.0}{3.4} = \frac{10}{17} \approx 0.5882, \quad d_{\text{peak}}(A, B) = 1 - \frac{10}{17} = \frac{7}{17} \approx 0.4118. \quad (125)$$

Route 2: Total-variation formulation. Work now at the level of the finite measures ν_A, ν_B rather than their individually normalized probability versions. The total-variation distance between ν_A and ν_B is

$$\text{TV}(\nu_A, \nu_B) := \frac{1}{2} \sum_{\omega \in \Omega} |\nu_A(\omega) - \nu_B(\omega)| \quad (126)$$

$$= \frac{1}{2} (|2.0 - 1.6| + |0.3 - 0.0| + |1.1 - 0.4|) \quad (127)$$

$$= \frac{1}{2} (0.4 + 0.3 + 0.7) = \frac{1}{2} \cdot 1.4 = 0.7. \quad (128)$$

The average total mass is

$$\frac{\|A\|_1 + \|B\|_1}{2} = \frac{3.4 + 2.0}{2} = 2.7, \quad (129)$$

so the normalized discrepancy

$$\delta := \frac{\text{TV}(\nu_A, \nu_B)}{\frac{1}{2}(\|A\|_1 + \|B\|_1)} = \frac{0.7}{2.7} = \frac{7}{27}. \quad (130)$$

The theoretical relationship between J_{peak} and this normalized total variation is

$$J_{\text{peak}}(A, B) = \frac{1 - \delta}{1 + \delta} = \frac{1 - \frac{7}{27}}{1 + \frac{7}{27}} = \frac{\frac{20}{27}}{\frac{34}{27}} = \frac{20}{34} = \frac{10}{17}, \quad (131)$$

which exactly matches the min–max computation above. The corresponding distance is

$$d_{\text{peak}}(A, B) = 1 - J_{\text{peak}}(A, B) = \frac{7}{17}, \quad (132)$$

again agreeing with Route 1.

This example confirms that the peak-to-peak similarity computed directly from magnitudes coincides with the expression obtained via total variation on the induced magnitude measures, provided we use the correct normalized discrepancy

$$\delta = \text{TV}(\nu_A, \nu_B) / \left(\frac{1}{2} (\|A\|_1 + \|B\|_1) \right) \quad (133)$$

rather than total variation between separately normalized probability distributions. Normalizing each signal to a unit-mass probability P_A, P_B would correspond to a different similarity notion, appropriate when we care only about shape and not about total magnitude.

5 Scalable Coherence Analysis for Large Ensembles

The Möbius inversion framework of Section 4 provides a complete $\mathcal{O}(2^m n)$ decomposition of magnitude for all 2^m coalitions of m signals. This is essential for detailed attribution and for understanding how mass is shared across specific subsets of signals. In contrast to this full 2^m -coalition expansion, which is intended for moderate m , many applications simply require a single, scalable $\mathcal{O}(mnK)$ coherence diagnostic: “*What fraction of the total dynamic range is agreed upon by all m signals simultaneously?*”

This question is answered directly by the Tanimoto similarity of the grand coalition of all signals. Let $[m] = \{1, \dots, m\}$ denote the index set and write $S_{\text{all}} = [m]$. Writing $\psi^{(K)}(A_j)$ for the multistate embedding of signal A_j , we define

$$J_{\text{peak}}(S_{\text{all}}) = \frac{N(S_{\text{all}})}{U_{\text{peak}}(S_{\text{all}})} = \frac{\sum_{\ell=0}^{K-1} \sum_{i=1}^n \min_{j \in S_{\text{all}}} [\psi^{(K)}(A_j)]_{i,\ell}}{\sum_{\ell=0}^{K-1} \sum_{i=1}^n \max_{j \in S_{\text{all}}} [\psi^{(K)}(A_j)]_{i,\ell}}. \quad (134)$$

The corresponding distance

$$d_{\text{peak}}(S_{\text{all}}) = 1 - J_{\text{peak}}(S_{\text{all}}) \quad (135)$$

quantifies the global disagreement, i.e., the fraction of the ensemble’s dynamic range that is *not* captured by unanimous, sign- and state-aware agreement across all m signals.

This $\mathcal{O}(mnK)$ grand-coalition measure provides a robust, scalable diagnostic even for large ensembles (for fixed K , the cost is $\mathcal{O}(mn)$). Furthermore, the per-index components of this disagreement,

$$M_i = \sum_{\ell=0}^{K-1} \left(\max_{j \in S_{\text{all}}} [\psi^{(K)}(A_j)]_{i,\ell} - \min_{j \in S_{\text{all}}} [\psi^{(K)}(A_j)]_{i,\ell} \right), \quad i = 1, \dots, n, \quad (136)$$

can be computed and sorted to pinpoint the coordinates i that contribute most to the ensemble's incoherence. In this way one obtains a global coherence score together with an index-wise incoherence profile, all without incurring the exponential cost of the full 2^m -coalition Möbius inversion.

6 Case Study

6.1 Sign-Aware Metrics: Phase-Shifted Signal Demonstration

Consider a synthetic sine wave $A_i = \sin(2\pi t_i/T)$ and a lagged version $B_i = \sin(2\pi(t_i - \Delta t)/T)$ sampled at $n = 400$ uniformly spaced points over one period T . For such signals, points near the zero-crossings exhibit sign mismatches as one signal leads or lags the other through zero.

For phase-shifted sinusoids, the Pearson correlation satisfies $r = \cos(\Delta\phi)$, where $\Delta\phi = 2\pi\Delta t/T$ is the phase shift. Thus, for a quarter-period shift $\Delta t = T/4$ (a 90° phase shift), $r = 0$, and for a smaller shift $\Delta t = T/12$ (a 30° phase shift), $r \approx 0.866$. The sign-aware Jaccard similarity J_{peak} responds differently: with a 90° shift we obtain $J_{\text{peak}} \approx 0.17$, so the signals retain some overlap where their signs coincide, even though their linear correlation is zero. For a 30° shift, we obtain $J_{\text{peak}} \approx 0.83$, reflecting strong sign-consistent agreement with milder penalties from misaligned zero-crossings.

Figure 1 summarizes the main ideas. **Panel (a)** displays the ingredients of the pairwise distance $d_{\text{peak}}(A, B)$ for the 90° phase shift: the green band marks the sign-consistent intersection $N(A, B)$, while the blue envelope traces the peak-to-peak union $U_{\text{peak}}(A, B)$ used for normalization. **Panel (b)** shows the multi-way additive breakdown $\tilde{N}(S)$ for three phase-shifted signals, illustrating how shared magnitude is partitioned among all coalitions.

Together, the panels demonstrate that the sign-aware framework (i) quantifies agreement strictly where signal polarities concur, (ii) penalizes phase shifts that induce sign reversals—behavior that ordinary correlation does not directly register, and (iii) decomposes total magnitude into non-overlapping contributions across multiple signals, enabling fine-grained interpretation of multi-signal relationships.

7 Conclusion: Distinctive Properties of the Peak-to-Peak Distance Family

The peak-to-peak distance family developed in this work combines several well-known mathematical structures: metric distances, positive-semidefinite kernels, probabilistic interpretations, and exact budget decompositions. None of these ingredients is new in isolation. What

Sign-Aware Peak-to-Peak Framework

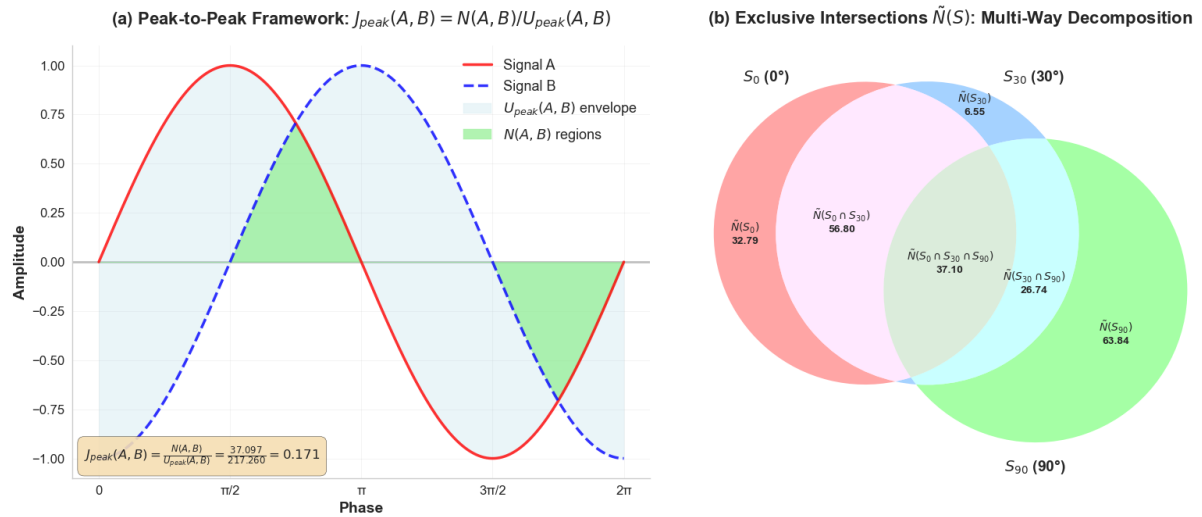


Figure 1: Visualization of the sign-aware peak-to-peak framework. **(a)** Components of the pairwise metric $d_{\text{peak}}(A, B)$ for Signal A ($\sin(2\pi t/T)$) and Signal B ($\sin(2\pi(t - \frac{T}{4})/T)$) with a 90° phase shift. The green shaded area represents the sign-aware intersection $N(A, B)$, and the light blue envelope shows the peak-to-peak union $U_{\text{peak}}(A, B)$ used for normalization. **(b)** Venn diagram illustrating the exclusive intersection components $\tilde{N}(S)$ for an ensemble of three signals with phase shifts 0° , 30° , and 90° , demonstrating the multi-way additive decomposition. Numerical labels are in arbitrary amplitude units with peak amplitude normalized to 1.

is distinctive is that they all arise from a single construction based on the sign-split embedding and its multistate extensions. We briefly summarize the resulting properties and their joint role in positioning d_{peak} among existing distance measures.

7.1 Synthesis of Multiple Mathematical Structures

The framework is built from three components: (i) the sign-split embedding ϕ , which maps signed signals to nonnegative representations while preserving magnitude; (ii) the multistate embeddings $\psi^{(K)}$ on user defined partitions of the real line; and (iii) the application of Tanimoto/Jaccard geometry to these embeddings. From this construction, the following properties emerge simultaneously.

Bounded, scale-free metric. The distance $d_{\text{peak}} : \mathbb{R}^n \times \mathbb{R}^n \rightarrow [0, 1]$ satisfies all metric axioms (Theorem 3.12). The $[0, 1]$ range makes distances comparable across datasets, and positive homogeneity implies scale invariance: for all $\alpha > 0$, $d_{\text{peak}}(\alpha A, \alpha B) = d_{\text{peak}}(A, B)$. This bounded, scale-free metric structure provides a robust foundation for clustering, hierarchical analysis, and other tasks that rely on well-behaved distances.

Positive-semidefinite kernel. The similarity coefficient J_{peak} defines a positive-semidefinite kernel $K_{\text{peak}} := J_{\text{peak}}$ (Theorem 3.15). For any finite collection of signals $\{A_1, \dots, A_m\}$, the Gram matrix $G_{ij} = K_{\text{peak}}(A_i, A_j)$ is positive semidefinite, enabling direct use in kernel SVMs, kernel PCA, Gaussian processes, and spectral methods without surrogate feature constructions. The same sign-aware geometry that defines the distance thus provides a valid kernel for standard ML pipelines.

Probabilistic semantics via normalized embeddings. Let $\Omega = \{1, \dots, n\} \times \{0, \dots, K-1\}$ denote the space of coordinate-state pairs. The multistate embedding $\psi^{(K)}(A)$ induces a finite measure ν_A on Ω with total mass $M_A = \|A\|_1$. Normalizing yields a probability distribution $P_A = \nu_A/M_A$ whenever $M_A > 0$. Proposition 4.12 shows that the discrepancy mass underlying d_{peak} is exactly $2\|\nu_A - \nu_B\|_{\text{TV}}$ and that

$$d_{\text{peak}}(A, B) = \frac{2\delta(A, B)}{1 + \delta(A, B)}, \quad \delta(A, B) := \frac{\text{TV}(\nu_A, \nu_B)}{\frac{1}{2}(M_A + M_B)}. \quad (137)$$

In the equal-mass case $M_A = M_B$, this reduces to a monotone transform of $\text{TV}(P_A, P_B)$. Thus similarity can be read directly in terms of total variation between induced distributions on Ω , and standard information-theoretic tools (e.g., data-processing under coarsening) apply.

Exact budget closure via Möbius inversion. Because ν_A is defined on a Boolean algebra of coordinate-state atoms, the framework admits an exact decomposition of each signal's magnitude across coalitions of signals via Möbius inversion (Definition 4.2). For a collection $\{A_1, \dots, A_m\}$, each L^1 norm satisfies

$$\|A_j\|_1 = \sum_{S \ni j} \widetilde{N}(S), \quad (138)$$

where the sum runs over coalitions containing j and each exclusive intersection $\widetilde{N}(S) \geq 0$. The decomposition is additive, unit-preserving, and non-overlapping: every unit of magnitude is assigned to exactly one coalition with no residual. This budget structure supports transparent ensemble analysis in settings where magnitude represents physical or monetary quantities that must be conserved.

Regime–intensity separation. The multistate embedding captures both which states are occupied and how much magnitude each state receives. At the pairwise level, agreement requires both state alignment (same bin) and comparable magnitudes within that state. Because Ω consists of disjoint coordinate–state atoms, the total discrepancy mass decomposes into two mutually exclusive mechanisms: cross-state contributions (regime shifts) and within-state contributions (intensification). This yields an exact global split

$$d_{\text{peak}}(A, B) = \pi_{\text{state}}(A, B) + \pi_{\text{mag}}(A, B), \quad (139)$$

where π_{state} measures how much distance is due to state changes and π_{mag} measures within-state intensity differences. In applications, this separation allows one to distinguish, for example, changes in temperature regimes from changes in heatwave intensity, or changes in spending baskets from changes in spending levels.

Conjunctive distinctiveness. Each of the properties above appears in some form in existing frameworks: cosine similarity and correlation provide kernels but lack metric structure and budget decompositions; L^1 and L^2 norms are metrics but ignore sign and do not yield PSD kernels or multistate budgets; Hellinger distance and Jensen–Shannon divergence are bounded and probabilistic but require probability inputs; Wasserstein distances encode geometry but are typically unbounded and do not provide additive budget partitions. The peak-to-peak family differs in that a single, sign-aware construction delivers *simultaneously* a bounded metric, a PSD kernel, probabilistic semantics linked to total variation, exact coalition budgets, and a built-in regime–intensity split for signed and complex signals.

7.2 Comparative Perspective

To situate d_{peak} within the broader landscape, we compared it with Wasserstein and Hellinger distances along axes such as boundedness, kernel structure, probabilistic interpretation, and budget behavior (Table 2). These two families represent mature, widely used paradigms in optimal transport and divergence-based statistics. Relative to them, the peak-to-peak distance trades some geometric flexibility (e.g., arbitrary ground metrics in Wasserstein) for a tightly integrated package of properties tailored to signed and multistate signals. We view this as complementary: d_{peak} provides a practical default when sign, regime, and magnitude budgeting are central, while classical distances remain appropriate when other structures dominate the modeling problem.

Table 2: Comparative properties of peak-to-peak, Wasserstein, and Hellinger distance families. Each row represents a mathematical property or application requirement, with entries describing whether and how each distance family satisfies that requirement. The peak-to-peak family is distinctive in simultaneously providing all listed properties within a unified construction operating directly on signed real-valued signals.

Property	Peak-to-peak d_{peak}	Wasserstein W_p	Hellinger H
Part I: Core mathematical properties			
(a) Bounded metric structure	Yes. Distance takes values in $[0, 1]$ for all signal pairs, providing scale-free comparisons. Satisfies the triangle inequality.	No in general. Boundedness requires the underlying ground space to have finite diameter. On \mathbb{R}^n with Euclidean metric, W_p is unbounded.	Yes. Distance takes values in $[0, 1]$ (or $[0, \sqrt{2}]$ depending on normalization). Satisfies the triangle inequality for probability measures.
(b) Positive semidefinite kernel	Yes. The similarity J_{peak} is a positive-semidefinite kernel on \mathbb{R}^n (Theorem 3.15), enabling direct use in SVMs, kernel PCA, and Gaussian processes.	No in general. While $e^{-\lambda W_p}$ can be positive-semidefinite for specific ground metrics and values of λ , this is not universal and typically requires case-by-case verification.	No. Related kernel available. While H itself is a metric rather than a kernel, the Bhattacharyya coefficient $k(p, q) = \sum_i \sqrt{p_i q_i}$ provides a related positive-semidefinite kernel.
(c) Probabilistic semantics	Yes. d_{peak} is a monotone transform of a normalized total variation $\delta(A, B)$ between the induced finite measures, with $d_{\text{peak}} = 2\delta/(1 + \delta)$ (Prop. 4.12). When $\ A\ _1 = \ B\ _1$, δ reduces to $TV(P_A, P_B)$.	Yes. Wasserstein distances quantify optimal transport cost between probability measures, with rich geometric and probabilistic interpretation.	Yes. Hellinger distance is a classical f -divergence with established probabilistic and information-theoretic foundations.

Table 2: Comparative properties of peak-to-peak, Wasserstein, and Hellinger distance families (continued).

Property	Peak-to-peak d_{peak}	Wasserstein W_p	Hellinger H
(d) Exact budget closure	Yes. Magnitude decomposes additively across coalitions via Möbius inversion: $\ A_j\ _1 = \sum_{S \ni j} N_f(S)$ with all terms non-negative (Proposition 4.4).	No. Transport cost does not admit additive decomposition into coalition contributions; the distance measures relocation effort rather than partitioning magnitude budgets.	No. While Hellinger distance can be expressed in terms of probability mass differences, it does not provide an additive budget partition structure.
Part II: Practical implementation properties			
(e) Mass and intensity control	Yes. Multistate channels capture categorical occupancy (mass distribution across states), while magnitude within channels captures quantitative intensity. Safe coarsening preserves structure (Proposition 4.7).	Partial. Captures mass relocation with geometric intensity via the ground metric (displacement distances), but does not employ explicit multistate channels with independent intensity control per channel.	Partial. Compares mass distribution across bins in a partition, but lacks a notion of geometric intensity or a built-in safe hierarchical coarsening of state structures.
(f) Extension to complex signals	Yes. Cartesian sign-split embedding treats real and imaginary parts independently. Polar embedding partitions phase angles (Definition 3.24).	Yes. One can define probability measures on (\mathbb{C}, d) for any metric d on the complex plane and compute Wasserstein distances between such measures.	Yes. Hellinger distance operates on any common measurable space, including \mathbb{C} with an appropriate σ -algebra.

Table 2: Comparative properties of peak-to-peak, Wasserstein, and Hellinger distance families (continued).

Property	Peak-to-peak d_{peak}	Wasserstein W_p	Hellinger H
(g) Collections and ensembles	Yes. Aggregate embeddings over collection members, normalize to P_S on coordinate-state atoms, compare via d_{peak} . Bounded, multiplicity-aware, budget-preserving, and robust to low-mass outliers.	Yes. Compare empirical or mixture measures induced by the collection. Leverages ground geometry and captures multiplicities, but lacks budget closure. Sensitivity and boundedness depend on the ground metric and domain.	Yes. Compare mixture distributions on a common σ -algebra. Bounded and multiplicity-aware, but ignores ground geometric structure. No budget closure or coalition decomposition.

The comparison in Table 2 reveals complementary strengths across the three distance families. Wasserstein distances excel in scenarios where the underlying geometry of the measurement space plays a central role, such as comparing images (where pixel displacement matters) or analyzing distributions on manifolds. The optimal transport framework provides elegant theoretical connections to convex analysis, partial differential equations, and Riemannian geometry. However, this geometric richness comes at the cost of computational complexity (generally requiring the solution of a linear program for discrete measures, or iterative approximation schemes) and the absence, in the generic setting, of certain algebraic structures (bounded range on unbounded domains, positive-semidefinite kernels, budget closure) that are essential for some applications. Hellinger distance, along with other f -divergences, provides computationally efficient bounded metrics between probability distributions with strong information-theoretic foundations, but it operates on pre-specified probability measures rather than directly on signal data, and it lacks the budget decomposition structure for coalition analysis.

The peak-to-peak family occupies a distinct niche by providing a complete suite of properties—metric structure, kernel structure, probabilistic semantics, and budget accounting—in a computationally straightforward framework that operates directly on raw signal data (real- or complex-valued, single signals or ensembles) without requiring explicit probability specifications or geometric ground metrics. This makes d_{peak} particularly well-suited for applications where signals carry physical units (financial returns, atmospheric fluxes, temperature anomalies, spectral coefficients), where both magnitude and directionality matter, where exact accounting is required for interpretability or regulatory compliance, and where kernel-based machine learning methods will be applied to the resulting similarity structure.

Acknowledgements

The research was carried out at the Jet Propulsion Laboratory, California Institute of Technology, under a contract with the National Aeronautics and Space Administration (80NM0018D0004).

References

- Bajusz, D., Rácz, A., and Héberger, K. (2015). Why is Tanimoto index an appropriate choice for fingerprint-based similarity calculations? *Journal of Cheminformatics*, 7(1):20. Article 20.
- Bouchard, M., Jousselme, A.-L., and Doré, P.-É. (2013). A proof for the positive definiteness of the jaccard index matrix. *International Journal of Approximate Reasoning*, 54(4):615–626.
- Bray, J. R. and Curtis, J. T. (1957). An ordination of the upland forest communities of southern Wisconsin. *Ecological monographs*, 27(4):325–349.
- Broder, A. Z. (1997). On the resemblance and containment of documents. In *Compression and Complexity of Sequences 1997 (SEQUENCES '97)*, pages 21–29. IEEE.
- Cha, S.-H. (2007). Comprehensive survey on distance/similarity measures between probability density functions. *City*, 1(2):1.
- Czekanowski, J. (1909). Zur Differentialdiagnose der Neandertalgruppe. *Korrespondenzblatt der Deutschen Gesellschaft für Anthropologie, Ethnologie und Urgeschichte*, 40:44–47.
- Gower, J. C. and Legendre, P. (1986). Metric and euclidean properties of dissimilarity coefficients. *Journal of Classification*, 3(1):5–48.
- Jaccard, P. (1901). Étude comparative de la distribution florale dans une portion des alpes et des jura. *Bulletin de la Société Vaudoise des Sciences Naturelles*, 37:547–579.
- Kosub, S. (2016). A note on the triangle inequality for the jaccard distance. *arXiv preprint arXiv:1612.02696*.
- Kosub, S. (2019). A note on the triangle inequality for the jaccard distance. *Pattern Recognition Letters*, 120:36–38.
- Kulczyński, S. (1927). Die pflanzenassoziationen der pieninen. *Bulletin International de l'Académie Polonaise des Sciences et des Lettres, Classe des Sciences Mathématiques et Naturelles, B (Sciences Naturelles)*, II:57–203. Also issued as an offprint: Cracovie, Imprimerie de l'Université, 1928.
- Levin, D. A., Peres, Y., and Wilmer, E. L. (2017). *Markov Chains and Mixing Times*. American Mathematical Society, Providence, RI, 2 edition.

- Mahalanobis, P. C. (1936). On the generalised distance in statistics. *Proceedings of the National Institute of Sciences of India*, 2(1):49–55.
- Marczewski, E. and Steinhaus, H. (1958). On a certain distance of sets and the corresponding distance of functions. In *Colloquium Mathematicum*, volume 6, pages 319–327. Instytut Matematyczny Polskiej Akademii Nauk.
- Motyka, J. (1947). O celach i metodach badań geobotanicznych [sur les buts et les méthodes des recherches géobotaniques]. *Annales Universitatis Mariae Curie-Skłodowska, Sectio C, Supplementum II*.
- Ralaivola, L., Swamidass, S. J., Saigo, H., and Baldi, P. (2005). Graph kernels for chemical informatics. *Neural Networks*, 18(8):1093–1110.
- Rogers, D. J. and Tanimoto, T. T. (1960). A computer program for classifying plants. *Science*, 132(3434):1115–1118.
- Rota, G.-C. (1964). On the foundations of combinatorial theory. i. theory of möbius functions. *Z. Wahrscheinlichkeitstheorie und Verwandte Gebiete*, 2:340–368.
- Ruzicka, M. (1958). Anwendung mathematisch-statistischer methoden in der geobotanik (synthetische bearbeitung von aufnahmen). *Biologia, Bratislava*, 13:647–661.
- Sakoe, H. and Chiba, S. (1978). Dynamic programming algorithm optimization for spoken word recognition. *IEEE Transactions on Acoustics, Speech, and Signal Processing*, 26(1):43–49.
- Salton, G. and McGill, M. J. (1983). *Introduction to Modern Information Retrieval*. McGraw–Hill.
- Schoenberg, I. J. (1935). Remarks to maurice fréchet's article "sur la définition axiomatique d'une classe d'espaces vectoriels distanciés applicables vectoriellement sur l'espace de hilbert". *Annals of Mathematics*, 36:724–732.
- Schölkopf, B. and Smola, A. J. (2002). *Learning with Kernels: Support Vector Machines, Regularization, Optimization, and Beyond*. MIT Press, Cambridge, MA.
- Swain, M. J. and Ballard, D. H. (1991). Color indexing. *International journal of computer vision*, 7(1):11–32.
- Tanimoto, T. T. (1958). An elementary mathematical theory of classification and prediction. Ibm technical report, International Business Machines Corporation, New York. Internal report, 10 pp.
- Tripp, A. et al. (2023). Tanimoto random features for scalable molecular machine learning. <https://arxiv.org/abs/2306.14809>.
- Villani, C. (2009). *Optimal Transport: Old and New*, volume 338 of *Grundlehren der mathematischen Wissenschaften*. Springer.

© 2025 California Institute of Technology